

1 **Net-Exchange parameterization of thermal infrared**
2 **radiative transfer in Venus' atmosphere**

V. Eymet¹

R. Fournier¹

J.-L. Dufresne²

S. Lebonnois²

F. Hourdin²

M.A. Bullock³

LAboratoire PLAsma et Conversion de l'Energie (LAPLACE), CNRS-UPS (UMR 5213),
Toulouse (France)

¹LAboratoire PLAsma et Conversion de

3 **Abstract.** Thermal radiation within Venus atmosphere is analyzed in close
4 details. Prominent features are identified that are then used to design a pa-
5 rameterization (a highly simplified and yet accurate enough model) to be used
6 in General Circulation Models. The analysis is based on a net-exchange for-
7 mulation, using a set of gaseous and cloud optical data chosen among avail-
8 able referenced data. The accuracy of the proposed parameterization method-
9 ology is controlled against Monte-Carlo simulations, assuming that the op-
10 tical data are exact. Then, the accuracy level corresponding to our present
11 optical data choice is discussed by comparison with available observations,
12 concentrating on the most unknown aspects of Venus thermal radiation, namely
13 the deep atmosphere opacity and the cloud composition and structure.

l'Energie (LAPLACE), CNRS-UPS (UMR
5213), Toulouse (France)

²Laboratoire de Météorologie Dynamique
(LMD-IPSL), CNRS-UPMC (UMR 8359),
Paris (France)

³Department of Space Studies, Southwest
Research Institute, Boulder, Colorado
(U.S.A)

1. Introduction

14 In the past decades, General circulation models (GCMs) have become central tools for
15 the study of the Earth climate and operational weather forecast. Because those numerical
16 tools are mainly based on physics laws, they can be in principle adapted quite easily to
17 various planetary atmospheres, by changing in particular fundamental parameters such
18 as the planetary radius, the gas heat capacity, etc. Some specific processes must also
19 be included depending on the planet such as the presence of ocean and of vegetation on
20 Earth, the CO₂ condensation on Mars, or the presence of photochemical haze surrounding
21 the atmosphere on Titan [*Hourdin et al.*, 1995; *Forget et al.*, 1999; *Richardson et al.*, 2007].
22 But a major step in this process is generally the development of a radiative transfer code.
23 Because of the complexity of radiative transfer computation, and because heating rates
24 must be computed typically a few times per hour for simulations covering decades or
25 centuries, at each mesh of a grid of typically a few tens of thousands of points, such
26 codes (named radiative transfer parameterizations) must be based on highly simplified
27 algorithms that are generally specific to the particular atmosphere.

28 From this point of view, the case of Venus is quite challenging. With its deep atmosphere
29 of CO₂ (92 bars at the surface), its huge greenhouse effect (735 K at surface), its H₂SO₄
30 clouds which in some spectral regions behave as pure scatterers, allowing to "see" through
31 the clouds in some near infrared windows [*Allen and Crawford*, 1984; *Bézard et al.*, 1990],
32 and because part of the spectral properties are not measured or constrained in the condi-
33 tions encountered there, Venus is even a problem for making reference computations with
34 line-by-line codes.

35 A full description of the energy balance of the atmosphere of Venus can be found in
36 *Titov et al.* [2007]. A large fraction of the solar flux is reflected by the clouds, allowing the
37 absorption by the atmosphere of only approximately 160 W m^{-2} on average. Only 10%
38 of the incident solar flux reaches the surface. Because of the thickness of the atmosphere
39 in most of the infrared, most of the outgoing thermal radiation comes from the cloud
40 top. Below clouds, the deeper atmosphere can only radiate to space in the near-infrared
41 windows. The huge infrared opacity in that region induces a strong greenhouse effect that
42 can explain the extremely hot surface temperature. In this region, energy is radiatively
43 transported through short-range radiative exchanges. Convection, essentially located in
44 the lower and middle clouds (from roughly 47-50 km to around 55 km altitude), has been
45 identified thanks to the stability profiles measured by Pioneer Venus and Venera entry
46 probes [*Schubert*, 1983]. This convection certainly plays a role in transporting energy
47 from the base of the clouds (heated from below by the deep atmosphere) to the upper
48 clouds, where infrared radiation is able to reach space. This one-dimensional description
49 of the energy balance is a global average view, and its latitudinal variations is related to
50 the dynamical structure of the atmosphere, the description of which is the main goal of a
51 General Circulation Model.

52 In order to perform reference infrared computations and to develop a fast algorithm
53 suitable for a GCM, we make use of the Net-Exchange Rate (NER) formalism based on
54 ideas originally proposed by *Green* [1967] and already used to derive a radiation code for
55 the LMD Martian GCM [*Dufresne et al.*, 2005], or to analyze the radiative exchanges on
56 Earth [*Eymet et al.*, 2004]. In the NER approach, rather than computing the radiative
57 budget as the divergence of the radiative flux, this budget is computed from the radiative

58 net-exchanges between all the possible pairs of elements A and B , defined as the difference
59 of the energy emitted by A and absorbed by B and that emitted by B and absorbed by
60 A . Using the plane parallel approximation, net radiative exchanges to be considered are
61 those between two atmospheric layers, between a surface and an atmospheric layer (space
62 being considered as a particular "surface" at 0K) or between the two surfaces (ground and
63 space). This formalism insures some important properties such as the reciprocity principle
64 and the energy conservation whatever the retained numerical assumptions [*Dufresne et al.*,
65 2005]. Thus, drastically different levels of approximation can be applied to various terms
66 of the computation, without violating those fundamental physical principles.

67 Within the GCM, the radiative transfer is divided in solar radiative forcing, and thermal
68 radiation energy redistribution (and cooling to space). This paper describes exclusively
69 how we use the NER formalism to compute thermal radiation, and how this computation
70 is parameterized for use within the GCM. This is only a first step, since we need also
71 to compute the solar radiative forcing with consistent input parameters (essentially the
72 cloud structure and optical properties) to get a fully consistent radiative scheme in the
73 GCM. But for the moment, the solar forcing in the GCM is taken from computations by
74 *Crisp* [1986], or from *Moroz et al.* [1985] and *Tomasko et al.* [1980]. The development of
75 a parameterization of solar forcing is a work in progress, and will be published in a future
76 paper.

77 In Section 2, a set of referenced optical data is chosen and briefly described for all
78 components of Venus atmosphere, and these optical data are used to perform reference
79 net-exchange simulations. The corresponding net-exchange matrices are then physically
80 interpreted, in order to highlight the features that will serve as start basis for the param-

81 eterization design. This parameterization is described and validated in Section 3. In the
82 validation process, accuracy is checked against reference Monte Carlo simulations assum-
83 ing that all optical data are exact. This means that, at this stage, the parameterization
84 methodology (the retained physical pictures, the formulation choices) is validated. In
85 particular, we can confidently extrapolate that no further technical developments will be
86 required if we want to include more accurate optical data that may arise from a better
87 knowledge of the spectral characteristics and composition of the atmosphere of Venus. But
88 we need to discuss the level of confidence associated to our present optical data against
89 available observations in order to allow an immediate use of the proposed parameterization
90 in Venus GCMs[*Lebonnois et al.*, 2005, 2006]. This discussion is the object of Section 4,
91 in which a particular attention is devoted to the collision induced continuum model and
92 the composition and vertical structure of the cloud.

2. Reference Net-Exchange simulations

2.1. Gas spectroscopic data

93 The temperature at ground level on Venus is $735 \pm 3\text{K}$ for a ground pressure of 92
94 ± 2 bar. The lower atmosphere is composed mainly of CO_2 (96.5%) and N_2 (3.5%)
95 that are well mixed over the whole atmosphere. In addition, Venus' atmosphere includes
96 several chemically active species: H_2O , CO , OCS , SO_2 , HCl and HF . Figure 1 displays the
97 concentrations used in our simulations. These concentrations are taken from the Venus
98 International Reference Atmosphere (VIRA)[*Seiff et al.*, 1985; *vonZahn and Moroz*, 1985],
99 and are consistent with the most recent reviews discussing Venus atmospheric composition
100 [*Taylor et al.*, 1997; *de Bergh et al.*, 2006; *Bézard and de Bergh*, 2007]. These reference
101 concentrations are used throughout the present document, keeping in mind that spatial

102 and temporal variabilities of reactive species remain widely unknown [*Taylor et al.*, 1997;
103 *Bézard and de Bergh*, 2007]. More recent observations are becoming available from the
104 Venus Express mission, in particular in the mesosphere [*Belyaev et al.*, 2008; *Fedorova*
105 *et al.*, 2008]. These new results should allow to define more precisely the reference profiles
106 used for future computations.

107 In the infrared domain, gaseous absorption is mainly due to rotation-vibration absorp-
108 tion lines of CO₂, H₂O, SO₂, CO, OCS, HDO, H₂S, HCl and HF. Because of the large
109 pressure variations with altitude, line widths are strongly dependent on altitude: from
110 very narrow isolated lines at the top of the atmosphere, to extremely wide lines with
111 strong line overlap in the deep atmosphere (see Fig. 2). At each altitude and for the
112 considered spectral interval, the average value \bar{k}_a of the absorption coefficient and the
113 overlap parameter Φ are also shown in Fig. 3. The overlap parameter Φ is defined as
114 $\Phi = \frac{\bar{k}_a^2}{k_a^2 - \bar{k}_a^2}$ where $k_a^2 - \bar{k}_a^2$ is the variance of the absorption coefficient within the spectral
115 interval. The variation of Φ with altitude is shown, for instance, in the [4700 – 4900]cm⁻¹
116 spectral interval (values of Φ may be different in a different spectral interval). Spectral
117 lines are well separated at high altitude and the overlap parameter Φ is small compared
118 to unity (Fig. 2a and 2b). Pressure broadening increases lines overlap at middle altitudes
119 (Fig. 2c) and, at the bottom of the atmosphere, lines can no longer be identified.

120 In the following simulations and quantitative analysis, gas absorption opacities are those
121 of *Bullock and Grinspoon* [2001]. These opacities were generated from high-resolution
122 spectral data for the nine main molecular species corresponding to a combination of the
123 HITRAN1996 and HITEMP line-by-line databases [*Rothman et al.*, 2000, 2003]. Contin-
124 uous absorption line spectra at each of 81 altitudes are reduced to discrete k-distribution

125 data sets [*Goody et al.*, 1989; *Lacis and Hansen*, 1991] on the basis of a narrow-band
126 spectral discretization and a 8 points Gaussian quadrature. The infrared spectrum from
127 1.71 to 250 μm (40 to 5700 cm^{-1}) is covered with 68 narrow bands. A description of
128 the corresponding spectral meshes can be found in table 3 (appendix A). The vertical
129 grid is regular: each atmospheric layer is 1km thick from the ground up to an altitude of
130 61km, and layers above this altitude are 2km thick. In order to account for the variation
131 with temperature of line intensities and line profiles, three distinct k-distribution data
132 sets have been computed : a primary set corresponding to the VIRA temperature profile
133 (referred to as T^{VIRA}) and two sets corresponding to a uniform 10 K increase and decrease
134 ($T^{VIRA} + 10 \text{ K}$ and $T^{VIRA} - 10 \text{ K}$ respectively).

135 Because of the high pressure and temperature levels encountered in Venus atmosphere,
136 collisions between gas molecules induce significant additional opacities. Compared with
137 standard absorption line spectra, these opacities evolve slowly with frequency and they are
138 commonly referred to as “collision-induced continuum”. This phenomenon is accurately
139 quantified for Earth atmosphere, but remains widely unknown as far as Venus atmosphere
140 is concerned. Hereafter, we only consider CO_2 - CO_2 collisions and we make use of modeling
141 results from A. Borysow¹ for the [10,250] cm^{-1} spectral range [*Gruszka and Borysow*, 1997]
142 together with available empirical data for the [250,4740] cm^{-1} spectral range [*Moskalenko*
143 *et al.*, 1979] (continuum is set to zero between 4740 and 5825 cm^{-1}). Another effect of high
144 pressures is to be found in the sub-Lorentzian nature of CO_2 absorption lines: absorption
145 in far wings is less than predicted by standard Lorentz pressure-broadened lines [*Burch*
146 *et al.*, 1969]. Correction factors are commonly used to account for this phenomenon
147 [*Bézard et al.*, 1990; *Perrin and Hartmann*, 1989], in particular in the so-called “spectral

148 windows” (mainly at 1.73 and 2.30 μm), but not enough experimental data are available
149 to allow quantitative evaluations throughout the all infrared spectrum, as required for the
150 present study. We therefore introduce no specific modification of the k-distribution data
151 set from *Bullock and Grinspoon* [2001], keeping in mind that line profiles were truncated
152 at 25 cm^{-1} from line center during its production.

153 Note that H_2O collision-induced continuum (*Roberts et al.* [1976], as presented in *Bullock*
154 [1997]), and Rayleigh scattering by CO_2 and N_2 with temperature and pressure depen-
155 dence of the real refraction index from the International Critical Tables [*Washburn et al.*,
156 1930] have also been included. Both phenomena have been shown to be negligible for the
157 purposes of the present study.

2.2. Clouds and hazes opacities

158 Venus is completely shrouded by clouds in the 47 to 70 km altitude region. Middle-
159 latitude clouds vertical structure and composition is known since measurements by *Venera*
160 9 and 10 landers, and the four entry probes from *Pioneer Venus* [*Esposito et al.*, 1983].
161 The cloudy region can be essentially subdivided into three distinct layers: the lower layer,
162 from 47 to 49 km, the middle from 49 to 57 km and the upper layer that extends from
163 57 km to the top of the clouds (70 km). Thinner hazes can be found above and below the
164 main cloud decks.

165 Cloud droplets are constituted by $\text{H}_2\text{SO}_4/\text{H}_2\text{O}$ aerosols [*Pollack et al.*, 1978]. Four dif-
166 ferent particle modes have been identified and their size distributions can be modeled
167 with truncated log-normal distributions [*Zasova et al.*, 2007; *Esposito et al.*, 1983; *Knol-*
168 *lenberg and Hunten*, 1980]. We retain here the modal properties and the nominal number
169 densities of *Zasova et al.* [2007] (see Table 1 and Table 2). These cloud microphysical

170 data and the complex refractive index of H₂SO₄ solutions [Palmer and Williams, 1975]
171 are used together with the Mie theory in order to compute the optical data required
172 for radiative transfer computations : total extinction optical depths, single-scattering
173 albedo and phase-functions. The detailed phase-function is not directly used. Instead, the
174 phase-function asymmetry parameter is computed on the basis of the exact Mie phase-
175 function and radiative transfer simulations are performed using the Henyey-Greenstein
176 phase-function [Goody and Yung, 1995]. Details of the clouds optical depths computation
177 can be found in appendix B. Figure 4 displays absorption and scattering coefficients while
178 Fig. 5 shows single-scattering albedo and asymmetry parameter as function of narrow-
179 band interval and atmospheric layer index. Note in particular that the single-scattering
180 albedo takes values very close to unity in the near-infrared ($\lambda < 2.5\mu m$), making the
181 clouds translucent and allowing thermal radiation from below to escape in the CO₂ spec-
182 tral windows.

2.3. Monte-Carlo simulations and Net-exchange rate analysis

183 The code KARINE ² is used together with the above presented gas and cloud spectral
184 databases to produce reference radiative transfer simulation results. This code is based
185 on a Net-Exchange Monte-Carlo algorithm. We will not describe here the details of such
186 algorithms, that were first introduced in *Cherkaoui et al.* [1996] and were gradually re-
187 fined in the last decade, in particular as far as atmospheric applications are concerned.
188 In the present context, it is particularly meaningful to point out the specific convergence
189 difficulties associated with extremely high optical thicknesses, for which practical solu-
190 tions were proposed recently, first for purely absorbing media [De Lataillade et al., 2002]
191 and then for simultaneous high absorption and high scattering conditions [Eymet et al.,

2005]. KARINE implements all such methodological developments and was submitted to
a systematic validation procedure against the corresponding benchmark solutions. Mul-
tiple scattering accurate representation was controlled with a specific attention using the
invariance properties of *Blanco and Fournier* [2003]; *Roger et al.* [2005].

Each radiative transfer simulation (and later, each parameterization call) produces a
Net-Exchange Rate (NER) matrix associated with the atmospheric vertical discretization
plus ground and space. The NER $\Psi(i, j)$ between two elements i and j of the atmosphere
(an element can be an atmospheric layer, ground or space) is defined as $E(j \rightarrow i)$, the
radiative power emitted by element j and absorbed by element i , minus $E(i \rightarrow j)$, the
radiative power emitted by element i and absorbed by element j [*Dufresne et al.*, 2005;
Green, 1967; *Joseph and Bursztyn*, 1976]. In the plane parallel approximation, each NER
between two atmospheric layers (or a layer and surface) has the dimension of a power per
surface unity (W/m^2). The radiative budget $\zeta(i)$ of element i is then the sum of NERs
between i and every other element j :

$$\Psi(i, j) = E(j \rightarrow i) - E(i \rightarrow j) \quad (1)$$

$$\zeta(i) = \sum_{j=0}^{m+1} \Psi(i, j) \quad (2)$$

The purpose of the present section is to physically analyze these NER matrices. To
avoid meaningless noisy structures, the NER analysis are performed on the basis of a
smoothed T^{VIRA} profile ³: a third order polynomial adjustment is made between the
surface and altitude $z = 43$ km on the basis of the original VIRA temperature profile (the
maximum temperature difference between T^{VIRA} and the adjusted profile is $\Delta T_{max} =$

211 2.5 K). Figure 6 displays the matrix of spectrally integrated NERs for this smoothed
212 temperature profile. NERs between a given atmospheric layer i and all other layers j can
213 be found on line index i . The line index 0 corresponds to ground, and line $m + 1 = 82$
214 to space. Let us take the example of layer number 30: elements of line number 30 show
215 first the NER between layer 30 and ground, then NERs between layer 30 and the 29
216 first atmospheric layers. These NER are positive: layer number 30 is heated by these 29
217 first layers because layer 30 is colder than layers below it. By definition, NER between
218 layer 30 and itself is null. Subsequent elements correspond to NERs between layer 30 and
219 atmospheric layers located above it, and the NER between layer 30 and space. These latter
220 NERs are negative because layer 30 is warmer than all above layers. The NER matrix
221 is antisymmetric because by definition $\Psi(j, i) = -\Psi(i, j)$, and all diagonal elements are
222 null: $\Psi(i, i) = 0$.

223 The amplitude of a given NER between two elements i and j is the result of the following
224 combined effects [*Eymet et al.*, 2004; *Dufresne et al.*, 2005] :

- 225 • temperature difference between i and j : the greater the temperature difference, the
226 greater the absolute value of the NER $\Psi(i, j)$;
- 227 • local emission/ absorption properties of i and j : maximum emission/ absorption is
228 reached when i or j behave like a blackbody, which is the case when i or j is either the
229 ground surface, space or an optically thick atmospheric layer (especially if the layer is
230 cloudy);
- 231 • attenuation of radiation along the optical paths between i and j : it depends on ab-
232 sorption properties of the intermediate atmosphere, distance between i and j , complexity
233 of the optical path domain in particular as far as multiple scattering is concerned.

234 In the case of Venus atmosphere, the temperature difference is quite easy to picture :
235 roughly speaking the greater the distance between i and j , the greater the temperature
236 difference. The two other points are more subtle because their influences are opposite as
237 function of absorption properties when i and/or j are gas layers : at frequencies where the
238 atmospheric gas is a strong absorber, the emission is strong, which increases the NERs
239 involving gas layers, but attenuation is also strong which decreases all types of distant
240 NERs. The strong spectral dependence of gaseous absorption (within or outside absorp-
241 tion bands, at the center or at the wings of absorption lines) is therefore essential when
242 physically analyzing the structure of the NER matrix of Fig. 6. Let us for instance
243 consider the NERs between gas layers in the deep atmosphere. Each gas layer can only
244 exchange radiation with its close neighbors. For further layers, although the tempera-
245 ture difference is greater, attenuation is too strong for significant net-exchanges to occur.
246 Above 10 km (layer index 12), although attenuation seems very strong from this point of
247 view, net-exchanges are observed with the bottom of the cloud (layers 49-50). This re-
248 quires that these two types of net-exchanges (with close neighbors and with cloud bottom)
249 occur at different frequencies within a given spectral band. The fact that NERs with the
250 cloud are observed is due to absorption by cloud droplets at frequencies where the atmo-
251 spheric gas alone would be quite transparent. The interpretation of the structure of the
252 NER matrix requires therefore to keep in mind the band structure of gaseous absorption
253 (see Fig. 3), the separated line structure within each band when pressure broadening is
254 not too strong (see Fig. 2) and the regularity of cloud absorption spectra (see Fig. 4).
255 The main features of Fig. 6 are the following :

256 • Net-exchanges between the ground (layer 0) and atmospheric layers is only significant
257 for the first layers. This is due to the extremely large opacities corresponding to 92 bars
258 of CO₂ at 700K. Pressure broadening is such that gaseous absorption lines are strongly
259 overlapped (see Fig. 2d), and no transmission at frequencies between lines centers is
260 possible: the gas behaves like an optically thick gray medium in each narrow band, as
261 indicated by the large values of the overlap parameter in Fig. 3b.

262 • Strong NERs are observed between neighboring layers up to 65 km. These intense
263 NERs, despite of small temperature differences (short distance NERs), indicate that even
264 at moderate pressures where the density of gaseous absorbers decreases, emission and
265 absorption are still very strong at the center of the most intense absorption lines.

266 • Long distance NERs between atmospheric layers are weak (the NER matrix is very
267 much empty), except as far as cloud layers are concerned (because of the continuous
268 absorption by cloud droplets).

269 • NERs with space are significant within and above the cloud region. This can be
270 analyzed similarly as the effect of cloud bottom for the deep atmosphere : space is a
271 “continuous absorber” that allows long distance net-exchanges in all spectral windows of
272 moderate gaseous absorption. This effect is particularly strong because space is at 3 K
273 and therefore temperature difference is large.

274 Further illustration of these mechanisms can be performed on the basis of partial NER
275 matrices corresponding to selected narrow bands. Fig. 7a and 7c display the NER ma-
276 trices corresponding to narrow bands index 1 and 6, that respectively cover the 1.73 μm
277 and 2.30 μm spectral windows. Net-exchanges between space and deep atmospheric lay-
278 ers (and even the ground) are clearly visible, as well as net-exchanges between distant

279 atmospheric layers within the deep atmosphere. Almost all NERs between space and the
 280 deep atmosphere occur in these two bands, which is the reason of their very specific role
 281 in terms of observations. Bands index 3 and 9 (Fig. 7b and 7d) are very different: optical
 282 thicknesses are high, and net-exchanges are strictly restricted to immediately adjacent gas
 283 layers.

284 For each narrow band, the total radiative budget of layer i in narrow band index nb

$$\zeta_{nb}(i) = \sum_{j=0}^{m+1} \Psi_{nb}(i, j) \quad (3)$$

285 can be decomposed also as

$$\zeta_{nb}(i) = \zeta_{nb}(i)^{atm-ground} + \zeta_{nb}(i)^{atm-space} + \zeta_{nb}(i)^{atm-atm} \quad (4)$$

286 where $\zeta_{nb}(i)^{atm-ground} = \Psi_{nb}(i, 0)$ is the net heating of layer i by the ground,
 287 $\zeta_{nb}(i)^{atm-space} = \Psi_{nb}(i, m + 1)$ is the opposite of the cooling to space of layer i and
 288 $\zeta_{nb}(i)^{atm-atm} = \sum_{j=1}^m \Psi_{nb}(i, j)$ is the portion of the radiative budget that is due to net-
 289 exchanges between atmospheric layer i and the rest of the atmosphere. Figure 8 displays
 290 these three contributions and the total radiative budget as function of wavelength and
 291 layer index i ⁴. It appears that :

- 292 • $\zeta_{nb}(i)^{atm-ground}$ (Fig. 8b) is null, except at the very bottom of the atmosphere.
- 293 • $\zeta_{nb}(i)^{atm-space}$ (Fig. 8c) is null for the whole deep atmosphere (except in the near-
 294 infrared windows where cooling to space occurs but is small compared with atm-atm
 295 exchanges) but the whole atmosphere above the clouds is significantly cooled by radiative
 296 exchanges with space. Cooling to space also occurs within the upper cloud and partially
 297 at the lower cloud levels through the rest of the cloud in some far-infrared spectral bands.

298 • $\zeta_{nb}(i)^{atm-atm}$ (Fig. 8d) is the dominant part of the radiative budget, except near
299 the surface and far above clouds. Generally speaking, the upper atmosphere is heated
300 by the deep atmosphere (which is reciprocally cooled by the same mechanism). atm-atm
301 net exchanges remain dominant above the clouds, in a region where the atmosphere is
302 optically thin enough for $\zeta_{nb}(i)^{atm-space}$ to be very significant in this very same region.
303 But again, this is due to the line structure of gaseous absorption: short distance atm-atm
304 net-exchanges occur at frequencies close to line centers, while long distance atm-space
305 net-exchanges are associated with line wing frequencies. Similar reasons lead to a atm-
306 atm net radiative cooling of most of the cloud (net-exchange with the upper part of the
307 cloud and the top atmosphere) that is comparable in magnitude with cooling to space.
308 Also very remarkable is the strong heating of the bottom of the cloudy region (layers
309 48-49) due to net-exchanges with the atmosphere below. Atm-atm net-exchanges are also
310 significant in the deep atmosphere.

311 The resulting vertical structure of the total radiative budget integrated over the whole
312 spectrum is displayed in Fig. 9. In the upper atmosphere (above 70 km),

313 Cooling to space dominates in the upper atmosphere (above 70 km), as well as in the
314 upper cloud region (57 to 70 km), with a marked maximum at 57 km (corresponding to
315 the upper limit of the dense cloud region). Within the dense cloud region (from 49 to 57
316 km) the net effect of atm-space and atm-atm net-exchanges is an overall net cooling of
317 the upper part, and a heating of the lower part (with a comparable magnitude). In the
318 center part of the dense cloud region, the structure of the radiative budget vertical profile
319 is quite complex, and is very sensitive to the temperature profile, which itself controls the
320 balance between solar heating, thermal exchanges and convection. The same observation

321 could be made in the deep atmosphere. In both cases, short distance atm-atm exchanges
322 are dominant, which means that the energy redistribution process associated with radia-
323 tion is close to a diffusion process : the medium is optically thick in terms of absorption
324 and a diffusive model such as Rosseland model is well adapted to the representation of
325 the combined effects of emission, absorption and scattering. In such a model, the total
326 radiative budget is proportional to the second derivative of the temperature profile with
327 altitude, and the present discretization in $m = 81$ layers, associated with the uncertain-
328 ties of the T^{VIRA} temperature profile, leads to strong fluctuations of this second order
329 derivative. These fluctuations are clearly visible in the middle of the cloud layer. Note
330 that when vertical energy exchanges are dominated by those local radiative exchanges,
331 the temperature adjusts so that the fluctuations disappear; but in the present uncoupled
332 study, the exchanges would have been dominated by those fluctuations if T^{VIRA} had not
333 been smoothed below 43km.

334 Finally, we show in Fig. 10 displays the differences between each reference NER (Fig. 6),
335 and NERs computed using the absorption approximation : absorption optical thicknesses
336 are unchanged, while both particulate scattering optical thicknesses and Rayleigh scatter-
337 ing optical thicknesses are set to zero. Scattering affects net exchanges between the base of
338 the clouds and the atmosphere underneath: radiation emitted in the bottom atmosphere
339 is partially reflected at the base of the cloud (backscattering effects). The same is true for
340 NERs between the upper atmosphere and the top of the dense cloud region, as well as for
341 NERs between all the atmosphere above the dense cloud region and space. Altogether,
342 the effect of scattering on the total radiative budget reaches 8% at the bottom and 7% at
343 the top of the dense cloud region (Fig. 9).

3. Parameterization

344 We derive a simple parameterization of the NER matrix usable in a general circulation
345 model. As a first step, we assume that the vertical distributions of infrared absorbers and
346 scatterers will be kept constant with latitude and time in the first phase of Venus general
347 circulation modeling. We therefore concentrate on the ability of the parameterization to
348 accurately represent the effects associated with temperature changes at constant compo-
349 sition. Corresponding computation requirements and extension to variable compositions
350 is then briefly discussed.

3.1. GCM parameterization simulations with constant atmospheric composition

351 For each NER $\Psi_{nb}(i, j)$ between elements i and j in narrow band index nb an exchange
352 factor $\bar{\xi}_{nb}(i, j)$ is defined, following *Dufresne et al.* [2005], as

$$\bar{\xi}_{nb}(i, j) = \frac{\Psi_{nb}(i, j)}{B_{nb}(j) - B_{nb}(i)} \quad (5)$$

353 where $B_{nb}(i)$ and $B_{nb}(j)$ are the values of the Planck function at the mass weighted average
354 temperatures \bar{T}_i and \bar{T}_j of atmospheric layers i and j respectively. The parameterization
355 objective is then to find efficient ways of evaluating $\bar{\xi}_{nb}(i, j)$. In the case of a constant
356 atmospheric composition, $\Psi_{nb}(i, j)$, and therefore $\bar{\xi}_{nb}(i, j)$, evolve as function of the atmo-
357 spheric temperature profile only. If we further assume that temperature variations around
358 the T^{VIRA} profile do not affect absorption and scattering cross sections, then tempera-
359 ture changes modify only the values of the Planck function and the sensitivity of $\bar{\xi}_{nb}(i, j)$
360 to temperature is strictly related to the vertical temperature profiles within atmospheric
361 layers i and j . In such conditions, as developed in *Dufresne et al.* [2005], we can argue

362 that a high level of accuracy is met by simply assuming that $\bar{\xi}_{nb}(i, j)$ takes a constant
 363 value $\bar{\xi}_{nb}^{ref}(i, j)$. NERs are evaluated as :

$$\Psi_{nb}(i, j) \approx \bar{\xi}_{nb}^{ref}(i, j) [B_{nb}(j) - B_{nb}(i)] \quad (6)$$

364 which only requires two computations of the Planck function at the average temperatures.
 365 The matrix of all $\bar{\xi}_{nb}^{ref}(i, j)$ is computed once for all using the Monte Carlo code detailed
 366 in the previous section.

367 There are three limit cases for which this approximation of a constant $\bar{\xi}_{nb}(i, j)$ may be
 368 demonstrated ⁵ :

- 369 1. when the absolute difference $|\bar{T}_i - \bar{T}_j|$ is large compared with the temperature vari-
 370 ations within atmospheric layers i and j (which corresponds essentially to the NERs
 371 between distant layers);
- 372 2. when atmospheric layers i and j are optically thin;
- 373 3. when atmospheric layers i and j are adjacent layers and the temperature profile is
 374 linear with pressure (or quadratic for adjacent layers of identical mass).

375 The reciprocity principle tells us that the space $\Gamma(i, j)$ of the optical paths γ from any
 376 point in atmospheric layer i to any point in atmospheric layer j is formally identical to
 377 the space $\Gamma(j, i)$ of the optical paths from any point in atmospheric layer j to any point
 378 in atmospheric layer i . This simply means that $E(i \rightarrow j)$ and $E(j \rightarrow i)$ (see Eq. 1) have
 379 the same integral structure [De Lataillade et al., 2002; Eymet et al., 2005; Dufresne et al.,
 380 1998] :

$$E(j \rightarrow i) = \int_{IR} d\nu \int_{\Gamma_{i,j}} d\gamma \xi_\nu(\gamma) B_\nu(\gamma, j) \quad (7)$$

$$E(i \rightarrow j) = \int_{IR} d\nu \int_{\Gamma_{i,j}} d\gamma \xi_\nu(\gamma) B_\nu(\gamma, i) \quad (8)$$

381 leading to

$$\Psi(i, j) = \int_{IR} d\nu \int_{\Gamma_{i,j}} d\gamma \xi_\nu(\gamma) [B_\nu(\gamma, j) - B_\nu(\gamma, i)] \quad (9)$$

382 where ν is the frequency integrated over the infrared, γ is the optical path integrated
 383 over the space $\Gamma(i, j)$, $\xi_\nu(\gamma)$ is an optico-geometric factor including absorption, scattering
 384 and surface reflection, and $B_\nu(\gamma, i)$ and $B_\nu(\gamma, j)$ are the blackbody intensities at the
 385 temperatures of the beginning and end of the optical path γ . With such a formulation the
 386 first limit case is trivial. Temperature variations within each layer can be neglected and
 387 the blackbody intensity difference $B_\nu(\gamma, j) - B_\nu(\gamma, i)$ in Eq. 9 can be approximated as
 388 $B_{nb}(j) - B_{nb}(i)$ (note that according to the narrow band assumption the Planck function
 389 is independent of frequency within each band) :

$$\Psi_{nb}(i, j) = \int_{\Delta\nu_{nb}} d\nu \int_{\Gamma_{ij}} d\gamma \xi_\nu(\gamma) [B_\nu(\gamma, j) - B_\nu(\gamma, i)] \quad (10)$$

$$\approx \left[\int_{\Delta\nu_{nb}} d\nu \int_{\Gamma_{ij}} d\gamma \xi_\nu(\gamma) \right] [B_{nb}(j) - B_{nb}(i)] \quad (11)$$

390 This means that

$$\bar{\xi}_{nb}(i, j) \approx \int_{\Delta\nu_{nb}} d\nu \int_{\Gamma_{ij}} d\gamma \xi_\nu(\gamma) \quad (12)$$

391 which depends on optical properties only and has therefore no direct temperature depen-
392 dence.

393 For the second limit case, the reason why $\bar{\xi}_{nb}(i, j)$ may be kept constant is that radiation
394 emitted at each location within a layer exits the layer without significant extinction. This
395 means that the total power emitted by a layer is the same as if the layer was isothermal
396 at a temperature corresponding to the average blackbody intensity. If the temperature
397 heterogeneity within each layer is small, the Planck function can be linearized and the
398 average blackbody intensity corresponds approximately to the Planck function at the
399 average temperature.

400 The third limit case is quite different, as no analogy can be made with the isothermal
401 layer case. The full demonstration can be found in *Dufresne et al.* [2005] and we only
402 concentrate here on the physical pictures corresponding to the particular case of optically
403 thick adjacent layers. As discussed in Section 2.3, radiative exchanges between adjacent
404 layers are indeed particularly important because they occur at frequencies where opacities
405 are high. At such frequencies the NER is dominated by optical paths corresponding to
406 radiation emitted and absorbed in the immediate vicinity of the interface between the two
407 layers. For such optical paths γ between layer i and layer $i + 1$, let us note $P_{\gamma,i}$ and $P_{\gamma,i+1}$
408 the pressure at the extremities of the path located in layer i and layer $i + 1$ respectively.
409 If $P_{\gamma,i}$ and $P_{\gamma,i+1}$ are close to the interface I the Planck function can be linearized as a
410 function of pressure :

$$B_\nu(\gamma, i) - B_\nu(\gamma, i + 1) \approx \left(\frac{\partial B_{nb}}{\partial P} \right)_I (P_{\gamma,i} - P_{\gamma,i+1}) \quad (13)$$

411 and the NER becomes

$$\Psi_{nb}(i, i+1) \approx \left[\int_{\Delta\nu_{nb}} d\nu \int_{\Gamma_{i,i+1}} d\gamma \xi_\nu(\gamma) (P_{\gamma,i} - P_{\gamma,i+1}) \right] \left(\frac{\partial B_{nb}}{\partial P} \right)_I \quad (14)$$

412 Provided that $\left(\frac{\partial B_{nb}}{\partial P} \right)_I$ can be replaced by the ratio $\frac{B_{nb}(i) - B_{nb}(i+1)}{P_{c,i} - P_{c,i+1}}$, we get

$$\bar{\xi}_{nb}(i, i+1) \approx \left[\int_{\Delta\nu_{nb}} d\nu \int_{\Gamma_{i,i+1}} d\gamma \xi_\nu(\gamma) (P_{\gamma,i} - P_{\gamma,i+1}) \right] \frac{1}{P_{c,i} - P_{c,i+1}} \quad (15)$$

413 where $P_{c,i}$ and $P_{c,i+1}$ are the pressure coordinates at the center of mass of layer i and layer
 414 $i+1$. As in the two first limit cases, $\bar{\xi}_{nb}(i, i+1)$ appears therefore as a purely optico-
 415 geometric quantity : it is independent of temperature despite of the fact that the sub-
 416 layer temperature profiles play an essential part in such exchanges. Replacing the Planck
 417 function gradient at the interface $\left(\frac{\partial B_{nb}}{\partial P} \right)_I$ by $\frac{B_{nb}(i) - B_{nb}(i+1)}{P_{c,i} - P_{c,i+1}}$ is exact if the Planck function
 418 can be linearized as function of temperature and if the temperature profile is either a
 419 linear function of P throughout the two adjacent layers (whatever layers thicknesses), or
 420 a quadratic function of pressure in the particular case where the two layers are of equal
 421 mass [*Dufresne et al.*, 2005].

422 These three limit cases are very much meaningful for the NERs that were shown to
 423 be dominant in Section 2.3 : NERs between adjacent layers on the one hand, and NERs
 424 with surface, space, cloud bottom and cloud top, on the other hand, that correspond to
 425 long distance exchanges for which the first and second limit cases apply. In order to test
 426 more generally the validity of the constant $\bar{\xi}_{nb}(i, j)$ assumption for Venus applications,
 427 we computed $\bar{\xi}_b^{ref}(i, j)$ for the VIRA profile and then computed the approximate solution
 428 (Eq. 6) and the exact solution for four perturbed temperature profiles. To obtain these
 429 profiles, we added sinusoidal temperature perturbations to the smoothed VIRA profile.

430 The amplitude of the perturbation is 10 K and the wavelength is 33 km. Four different
 431 phases are used in order to check the effects of changes in temperature and temperature
 432 gradients at all altitudes in the range of the maximum fluctuations expected in Venus
 433 GCMs: these four temperature profiles ($T_2 - T_5$) are: $T_2(z) = T^{VIRA}(z) + 10\sin\left(\frac{2\pi z}{33}\right)$,
 434 $T_3(z) = T^{VIRA}(z) - 10\sin\left(\frac{2\pi z}{33}\right)$, $T_4(z) = T^{VIRA}(z) + 10\sin\left(\frac{2\pi z}{33} - \frac{\pi}{2}\right)$, $T_5(z) = T^{VIRA}(z) -$
 435 $10\sin\left(\frac{2\pi z}{33} - \frac{\pi}{2}\right)$. Figure 11 displays such comparisons, indicating that the adequation is
 436 quasi perfect at all altitudes.

437 This parameterization is presently used in a first series of three-dimension Venus GCM
 438 simulations [*Eymet et al.*, 2006; *Crespin et al.*, 2006] based on the terrestrial LMDZ model
 439 [*Hourdin et al.*, 2006]. Such simulations include the surface pressure variations associ-
 440 ated with orography, which means that the $\bar{\xi}_{nb}^{ref}(i, j)$ matrix is different at each latitude-
 441 longitude location. In order to avoid the computation and storage of a large number of
 442 such matrices, $\bar{\xi}_{nb}^{ref}(i, j)$ is interpolated on the basis of 96 simulations corresponding to a
 443 regular discretization of surface pressures in the 40-115 bar range (using a 5 bars step) and
 444 a discretization of the altitude at the top of the clouds in the 58-70 km range (using a 4 km
 445 step). This is widely sufficient to meet the present requirements and no further efforts
 446 were made toward storage reduction, in particular as far as the number of narrow-bands
 447 is concerned.

448 Note that in the tests performed above (Fig. 11) we used infrared opacities correspond-
 449 ing to the reference T^{VIRA} profile. The variations of infrared opacities with temperature
 450 were therefore neglected. The effect of this approximation on cooling rates can be eval-
 451 uated, in order to check whether a parameterization refinement is required, using the
 452 k-distribution data built for temperature profiles shifted of +10 K and -10 K away from

453 T^{VIRA} (see section 2.1). A reference solution is built, in which k-distribution data are
454 linearly interpolated between $T^{VIRA} - 10$ K, T^{VIRA} and $T^{VIRA} + 10$ K and the results are
455 compared to the previous parameterization results. It appears that, in terms of cooling
456 rates, opacity variations with temperature have only significant influences ($\approx 10\%$) in the
457 high atmosphere above the clouds. A simple practical solution is detailed in appendix C
458 that allows the parameterization to be upgraded in order to correct this discrepancy (see
459 Fig. 12).

3.2. Computational requirements and extension toward variable cloud structures

460 In the current configuration, with 68 narrow bands and 50 vertical levels, the use of
461 this parameterization in the Venus version of LMDZ GCM, with one single NER matrix,
462 increases the size of the model executable from roughly 360 Mo to 425 Mo. To include
463 the surface pressure dependency, the use of 16 different matrices increases this size by
464 roughly 23 Mo. This increase is linear with respect to the number of matrices used, which
465 means that using N matrices would increase the size by roughly $1.5 \times N$ (in Mo). N
466 could therefore be significantly increased above 16 without any difficulty, which will first
467 be used to test the effect of the variations with latitude of cloud altitudes and structures.

468 Increasing the number of NER matrices can therefore be easily used to account for
469 spatial variations of the atmospheric composition, but a strong limitation of the present
470 proposition is the fact that composition is assumed constant in time. In a near future,
471 if the amounts of absorbers and scatterers (gaseous absorbers and cloud droplets) are
472 allowed to vary along a GCM simulation, then a physical model will be required for the
473 variation of $\bar{\xi}_{nb}^{ref}(i, j)$ with atmospheric composition. For large variations, the correspond-

474 ing computational requirements will probably be very significant and the first steps will
475 therefore be to find systematic ways of reducing the number of NERs by neglecting parts
476 of the matrix for a given accuracy level, optimize the number of narrow-bands, and lin-
477 earize the blackbody intensities with temperature (which allows a summation over the
478 narrow-bands as illustrated in Appendix C) without violating the reciprocity principle.
479 All such developments will be held successively, following the needs of the Venus GCM
480 community, and will probably concentrate on the cloud region and the upper atmosphere.

481 However, for small variations, simple solutions can be rapidly implemented. Each
482 $\bar{\xi}_{nb}^{ref}(i, j)$ can indeed be linearized as function of n main parameters of the vertical dis-
483 tributions of absorbers and scatterers. Such an approach only requires that sensitivity
484 matrices are computed once and stored for use in a Taylor like first order expansion. The
485 feasibility is therefore directly related to

- 486 • the computation time required to produce the sensitivity matrices with sufficient
487 accuracy level,
- 488 • the additional memory size corresponding the $n \times N$ sensitivity matrices (where, as
489 defined above, N is the number of reference NER matrices),
- 490 • and the computation time associated to the linear computation of each $\bar{\xi}_{nb}(i, j)$ from
491 $\bar{\xi}_{nb}^{ref}(i, j)$ and its sensitivities to the n retained parameters.

492 The computation of sensitivity matrices may look very demanding. It will indeed not be
493 possible to make use of analytical formulations of the NER sensitivities, because scatter-
494 ing is essential in the vicinity and within the cloud, where composition variations will first
495 be analysed (see Fig. 9 and Section 2.3). Accurately computing sensitivities of infrared
496 radiative transfer quantities with numerical tools is a well identified difficulty and very

497 few practical solutions are available [*Weise and Zhang, 1997*]. However it was recently
498 shown that such sensitivities could be computed with the Monte Carlo method, in parallel
499 to the main computation algorithm, with very little additional computation costs [*Roger*
500 *et al.*, 2005]. Upgrading KARINE to compute the sensitivities of $\bar{\xi}_{nb}^{ref}(i, j)$ to the vertical
501 composition parameters is therefore only a question of practical implementation (most of
502 the corresponding feasibility tests have already been performed by *Roger* [2006]). Com-
503 puting $n \times N$ with n and N of the order of several tens should therefore introduce no
504 specific technical difficulty. The above reported tests indicate that the memory size in-
505 crease should be of the order of $1.5 \times n \times N$ (in Mo). For the computers used in this study,
506 a memory size of up to 2 Go would be acceptable, which allows to reach $n \times N$ values of
507 the order of 1000. If we think of a maximum of $N = 30$ for variations with grid points
508 of orography and cloud structure, this leaves us with $n = 30$ parameters for the vertical
509 composition at each grid point, which should be widely sufficient for first analysis of the
510 coupling of atmospheric dynamics with chemistry (if radiation is indeed shown to play a
511 significant role in this coupling). In terms of computing time, the present configuration of
512 the parameterization (with 2000 radiative iterations per Venus day) induces an increase
513 of approximately 10% of the total computing time of the GCM. Including the sensitivities
514 to n parameters with n of the order of several tens may increase this proportion, though
515 this needs to be assessed.

4. Comparison with observations and sensitivity to the main free parameters

516 The new parameterization accuracy has been checked so far against Monte Carlo simu-
517 lation results assuming that all optical data are exact and we can confidently extrapolate
518 that the parameterization methodology will remain accurate if enhanced optical data are

519 used in the future. The purpose of the present section is to establish the uncertainty level
520 associated to our present data in order to allow their use in today's first series of GCM
521 simulations.

522 The easiest quantitative control consists in the computation of the emitted thermal
523 radiation at the top of the atmosphere and its comparison with the incident solar flux time
524 the integral Bond albedo. It is commonly admitted that the expected average emitted
525 flux should be $157 \pm 6 \text{ W m}^{-2}$ *Titov et al.* [2007]. Using the optical data and the
526 cloud structure described in Section 2, together with the VIRA temperature profile, we
527 obtain an emitted flux value of 156.0 W m^{-2} which is within the expected range. To
528 further analyse this emitted thermal radiation, its spectrum is first compared in Fig. 13
529 with the spectrum of blackbody emission at 232 K as suggested in *Bullock and Grinspoon*
530 [2001]. In logarithmic scale, the agreement is indeed very good, except in the strong CO_2
531 absorption bands and at near-infrared frequencies where the H_2SO_4 clouds are translucent.
532 The detailed spectral structure can then be compared with available observations. For
533 the $[0; 2000 \text{ cm}^{-1}]$ wavenumber range, Fig. 14 displays a comparison with the average
534 spectrum corresponding to the $[-10; +10]$ latitudes as observed during the Venera 15
535 mission (*Zasova et al.* [2007]). These data are retained here because *Zasova et al.* used
536 them to infer the cloud model that we retained for the present study. A high level of
537 consistency can therefore be expected, and indeed the two spectra match quite accurately.
538 This spectral signature is also very close to that of the emitted fluxes simulated by *Crisp*
539 *and Titov* [1997]; *Titov et al.* [2007] at a much higher spectral resolution ⁶. Comparison
540 with the simulation results of *Pollack et al.* [1980] is less satisfactory but the essential
541 features can still be considered quite similar, keeping in mind the limits of the gaseous

542 spectral data and the cloud models available in the early 80's. For the [2000; 4000 cm^{-1}]
543 wavenumber range, Fig. 15 displays a comparison with observations performed by the
544 NIMS instrument during the 1990 Galileo flyby of the dark side of Venus [*Carlson, 1991*;
545 *Taylor et al., 1997*]. The agreement is not as good as in Fig. 14 but is still very much
546 satisfactory considering our poor spectral resolution in this less energetic part of the
547 spectrum.

548 Similar spectral comparisons could not be performed for altitude levels within the atmo-
549 sphere because all available observed spectra correspond to outgoing radiation at the top
550 of the atmosphere. We could only compare our spectra with those simulated by *Pollack*
551 *et al.* [1980], as reported in Fig. 16: at the level corresponding to a pressure of 0.79 atm
552 the agreement is as partial as for the top of atmosphere flux, but again, absorption data
553 and cloud models are quite different. Further analysis of net-fluxes within the atmosphere
554 can only be performed on a spectrally integrated basis. Figure 17 displays the integrated
555 net flux as a function of altitude for our nominal model using VIRA temperature profile.
556 For comparison, Fig. 18 reproduces the net thermal flux derived from the SNFR and LIR
557 measurements on Pioneer Venus descent probes, as summarized in *Revercomb et al.* [1985].
558 The uncertainty and appearant dependance on location are such that these observations
559 are very difficult to use for the present validation exercise. However, we can keep in mind
560 that the order of magnitude of 100 Wm^{-2} at 60 km seems to be a point of agreement,
561 but none of the observed net flux profiles shows such a strong variation at the bottom
562 of the cloud as what we simulate with our optical data (from 20 Wm^{-2} to 60 Wm^{-2} in a
563 few kilometers when descending through the bottom of the cloud). An other discrepancy
564 is the net flux value in the very low atmosphere : in the bottom twenty kilometers, we

565 find net fluxes between $20Wm^{-2}$ and $50Wm^{-2}$, whereas measurements are more in the
566 $[0; 20Wm^{-2}]$ range.

567 This raises the question of continuum adjustment. The CO_2 continuum model that we
568 are using is very much uncertain. Some constraints are available in the near-infrared win-
569 dows, but at all other frequencies, specifications of the continuum can only be addressed
570 through modeling attempts, without any experimental control. Collision induced continu-
571 ums are much better understood for Earth-like conditions, but the pressure levels ($92bars$)
572 and the typical exchange distances ($1km$) encountered in the deep Venus atmosphere are
573 so high that no laboratory experiment is able to reproduce comparable conditions. The
574 collision induced continuum is therefore essentially unknown in the energetically dominant
575 part of the spectrum. Furthermore, the far wing sublorentzian shapes of absorption lines
576 at such pressures is also very much unknown and this induces a continuum-like uncer-
577 tainty that cannot be distinguished from the collision induced continuum. Some kind of
578 continuum adjustment is therefore required in any radiative simulation. Despite of the
579 measurement uncertainties, the above described comparison of simulated and observed
580 net-flux vertical profiles can help us in this adjustment exercise. In Fig. 17, simulated
581 net-flux profiles are reported that correspond to various scaling factors applied to our con-
582 tinuum model at all frequencies below $4030cm^{-1}$. The continuum is kept unchanged at
583 near infrared frequencies because this is the only frequency range for which the continuum
584 can be constrained on the basis of observed emitted spectra at the top of the atmosphere
585 (and we indeed checked that our continuum values were consistent with the values used
586 by *Bézard et al.* [1990] in the 1.73 and $2.30 \mu m$ spectral windows). The conclusions of this
587 sensitivity test to the continuum model is that we need to increase continuum absorption

588 by a factor as high as 6 if we want that the integrated net-flux be lower than $20Wm^{-2}$ at
589 $20km$. Doing so, the net-flux profile is only weakly modified within and above the cloud,
590 but the strong net flux variation at the bottom of the cloud is considerably reduced, which
591 leads to a better agreement with descent probes observations.

592 The other available data within the atmosphere are the observed and simulated solar net-
593 fluxes. In first approximation, these can be related to the thermal net-fluxes provided that
594 convection processes and atmospheric transport are negligible. Convection processes are
595 assumed to play a role within the cloud and at some locations in the deep atmosphere
596 and atmospheric transport is systematically mentioned when attempting to analyse the
597 observed latitudinal temperature contrasts. However, at most latitudes/altitudes, except
598 within the cloud, it remains very much meaningful to think of Venus atmosphere as in a
599 state of radiative equilibrium, or quite close to radiative equilibrium. The detailed analysis
600 of such processes is one of the objectives of GCM simulations, but we still briefly compare
601 here, in Fig. 17 the thermal net-flux profiles corresponding to our nominal model (with
602 the original continuum and the continuum increased by a factor 4 and then 6) with three
603 global mean net solar fluxes from the literature (*Tomasko et al.* [1980]; *Moroz et al.* [1985];
604 *Crisp* [1986]). All three thermal net flux profiles are compatible with $157 + / - 6Wm^{-2}$
605 at the top of the atmosphere. A convection zone is clearly visible between 48 and 55km,
606 since the thermal net flux is lower than the expected solar net flux. Orders of magnitude
607 between solar and thermal net fluxes are comparable in the lower atmosphere (below
608 48km) when continuum absorption optical depths are adequately adjusted. Note that,
609 should the continuum optical depth be multiplied by a factor 4 or 6, a convection zone
610 would appear in the ten first kilometers. Finally, differences between thermal and solar net

611 fluxes are clearly visible in the 55-65km zone, which may be due to the fact that different
612 cloud models were used for solar fluxes computations, or to 3D circulation effects, which
613 would imply that reasoning on the basis of a latitudinally averaged solar net flux profile
614 is meaningless.

615 Apart from collision-induced absorption, the most significant free parameters are the
616 parameters of the cloud model. These parameters are constrained by top of atmosphere
617 fluxes as well as in-situ observations of particle sizes and shapes along descent probes
618 trajectories. However, these constraints leave strong uncertainties concerning particle size
619 distributions and vertical density profiles, particularly at high latitudes where the cloud
620 structure can be considered as virtually unknown . A systematic sensitivity analysis
621 cannot be among the objectives of the present paper and we therefore only discuss four
622 sensitivity tests: successively, each particle mode of our nominal cloud model (that of
623 *Zasova et al.* [2007]) is replaced by that of *Knollenberg and Hunten* [1980]. Mode 2
624 particles exist only in the high cloud in *Zasova et al.* [2007], whereas they are present
625 throughout the whole cloud in *Knollenberg and Hunten* [1980]. Therefore, the curve
626 labeled “replacing mode 2” was obtained with a cloud model where mode 2 particles have
627 been taken from *Knollenberg and Hunten* [1980] for altitudes higher than 65km only.
628 Since there is no mode 2' particles in *Knollenberg and Hunten* [1980], the curve labeled
629 “mode 2' divided by 3” has been obtained with a cloud model where nominal mode 2'
630 cumulated optical depths at $0.63\mu\text{m}$, at 48km ($\tau_{0.63\mu\text{m}} = 14.26$) have been scaled to match
631 the data presented in *Tomasko et al.* [1985] ($\tau_{0.63\mu\text{m}} = 4.66$ at 48km), which required
632 that mode 2' particle densities were divided by a factor three. The result of these tests,
633 displayed in Fig. 19, indicate that sensitivities of the thermal net flux at the top of the

634 atmosphere are quite small. The largest differences (less than 10%) are obtained when
635 modifying mode 2 and 2' properties. Fig. 19(b) displays the differences between the
636 radiative budget corresponding to the modified clouds on the one hand and the nominal
637 radiative budgets of Fig. 9(a) on the other hand. Sensitivities to the cloud model are
638 much larger in terms of radiative budgets than in terms of top of the atmosphere fluxes:
639 differences are approximately 20% for modes 1, 2 and 2', and reach 50% for mode 3. These
640 impacts are concentrated in the cloud region and may significantly modify the convective
641 structure, and the details of the general circulation in the 40-70 km altitude range. It
642 is therefore important to consider introducing the dependency of the NER coefficients
643 to cloud parameters, together with the coupling of a microphysical model describing the
644 cloud structure within the GCM.

5. Conclusion and perspectives

645 Major progress in our understanding of planetary atmospheric systems require that
646 ground based or spatial observations are accompanied by the development of compre-
647 hensive models, which because of the complexity and non linearity of the atmospheric
648 dynamics and physics, can generally be achieved only through the development of physi-
649 cally based numerical tools such as the so called General Circulation Models. One major
650 step in the development of such models is the derivation of "radiative transfer parameter-
651 izations", i.e. highly simplified but accurate enough versions of the full radiative transfer
652 calculation. This major step in general, becomes a real challenge in the extreme venusian
653 case, with in particular its deep CO₂ atmosphere and highly scattering clouds.

654 We have presented in the present paper the process of the development of the radiative
655 transfer code which is presently operational in the LMD venusian GCM. Several results
656 have been achieved during this long process :

657 • It was first practically demonstrated that most recent Monte Carlo algorithms were
658 able to accurately simulate infrared radiative transfer in such an optically thick system as
659 Venus atmosphere (in terms of both absorption and scattering). Because of their integral
660 nature, the NERs considered in the present work could only be evaluated with integral
661 radiative transfer solvers, and among them only the Monte Carlo algorithms can deal with
662 low Knudsen multiple scattering. This step was therefore essential.

663 • The Venus NER matrices were carefully analysed prior to any parameterization at-
664 tempt. We believe that the corresponding physical pictures may provide usefull insights to
665 Venus radiative transfer, particularly when attempting to analyse the coupling of radiation
666 with atmospheric dynamics.

667 • An essential point was the quantification of the impact of the main remaining un-
668 certainty sources. We concentrated on collision induced continuum and cloud particle
669 vertical distributions, for which we show that significant changes in optical properties
670 may have little impacts on the well constrained top of atmosphere fluxes, but strong im-
671 pacts on very much unknown radiative energy exchanges as well as radiation-convection
672 vertical coupling. The fact that few direct observations are available concerning contin-
673 uum absorption and detailed cloud structures leaves strong degrees of freedom that must
674 be translated into adjustable parameters when trying to reproduce Venus vertical thermal
675 structure and atmospheric dynamics with a general circulation model.

676 • When exploring optical data available in the literature, we observed that it was very
677 difficult to distinguish between differences that are worth a detailed physical interpre-
678 tation attempt, and differences that are only the consequences of inversion procedure
679 uncertainties. This can be easily explained by the strong difficulties associated to the
680 understanding of such a complex physical system as Venus atmosphere. Obviously the
681 state of the art is undeniably more advanced and clearer as far as near-infrared windows
682 are concerned, but we can state that detailed general circulation analysis will require that
683 strong further efforts be made toward the representation of optical properties throughout
684 the whole infrared at all altitudes.

685 • Finally, at our given stage of knowledge, we have shown that it was possible to
686 derive, thanks to the NER approach, and despite the extreme conditions encountered
687 in the venusian atmosphere, a fast and accurate parameterization usable in a GCM.
688 Of course, the methodology can be used to update the radiative code, as soon as new
689 information becomes available on the venusian atmospheric composition, microphysical
690 cloud properties and optical properties.

691 Until now, the code was only derived for a fixed atmospheric composition and for
692 thermal radiation only. Accounting to first order to the space time variations of clouds
693 or composition is not a major issue, and should be considered in the future, when the
694 question will arise from the climate studies. We are currently working on the derivation
695 of a code for the shortwave radiation.

696 **Acknowledgments.** This work has been supported by the Centre National d'Etudes
697 Spatiales (CNES). V.E. acknowledges support from ESA 18134/04/NL/LVH/GM and

698 from the postdoctoral fellowship program of CNES. M.B. acknowledges support from
699 NASA Planetary Atmospheres grant NNG06GD61G.

Notes

- 700 1. <http://www.astro.ku.dk/~aborysow>
2. <http://web.lmd.jussieu.fr/~eymet/karine.html>
3. As the lower atmosphere is highly absorbing, IR radiative transfer has Rosseland-like diffusive features and fluctuations on a discretized temperature profile induce apparent second order spatial derivatives that translate into strong net exchanges between adjacent layers.
4. In all figures displaying radiative budgets of atmospheric layers, results are presented in W/m^3 , corresponding to $\zeta_{nb}(i)/\Delta z_i$, where Δz_i is the thickness of layer i . This allows quantitative comparisons independantly of the vertical discretization. This transformation cannot be used when analysing Net-exchange matrices (see figures 6 and 7 where results are presented in W/m^2), because each net-exchange involves two atmospheric layers.
5. the discussion assumes that i and j are atmospheric layers, but extension to cases where i or j is ground or space is straightforward
6. This result is not reproduced in Fig. 14, but the agreement level is very much similar to that of comparisons with *Zasova et al.* [2007] results.

References

- 701 Allen, D., and J. Crawford (1984), Cloud structure on the dark side of Venus, *Nature*,
702 *307*, 222–224.
- 703 Belyaev, D., O. Korablev, A. Fedorova, J.-L. Bertaux, A.-C. Vandaele, F. Montmessin,
704 A. Mahieux, V. Wilquet, and R. Drummond (2008), First observations of SO₂ above
705 Venus' clouds by means of solar occultation in the infrared, *JGR*, *113*, E00B25, doi:
706 10.1029/2008JE003143.
- 707 Blanco, S., and R. Fournier (2003), An invariance property of diffusive random walks,
708 *Europhysics Letter*, *61* (2), 168–173.
- 709 Bullock, M. (1997), The stability of climate on Venus, Ph.D. thesis, University of Colorado.

710 Bullock, M., and D. Grinspoon (2001), The recent evolution of climate on Venus, *Icarus*,
711 *150*, 19–37.

712 Burch, D., D. Gryvnak, R. Patty, and C. Bartky (1969), Absorption of infrared radiant
713 energy by CO_2 and H_2O . iv. shapes of collision-broadened CO_2 lines, *Journal of the Optical*
714 *Society of America*, *59*, 267–280.

715 Bézard, B., and C. de Bergh (2007), Composition of the atmosphere of Venus below the
716 clouds, *JGR*, *112*, E04S07, doi:10.1029/2006JE002794.

717 Bézard, B., C. de Bergh, D. Crisp, and J. Maillard (1990), The deep atmosphere of Venus
718 revealed by high-resolution nightside spectra., *Nature*, *345*, 508–511.

719 Carlson, R. e. a. (1991), Galileo infrared imaging spectroscopy measurements at Venus,
720 *Science*, *253*, 1541–1548.

721 Cherkaoui, M., J. L. Dufresne, R. Fournier, J. Y. Grandpeix, and A. Lahellec (1996),
722 Monte-Carlo simulation of radiation in gases with a narrow-band model and a net-
723 exchange formulation, *ASME Journal of Heat Transfer*, *118*, 401–407.

724 Crespin, A., S. Lebonnois, F. Hourdin, V. Eymet, R. Fournier, and F. Forget (2006), An
725 infrared radiative transfer parameterization for a Venus General Circulation Model, in
726 *DPS meeting, 2006, B.A.A.S. 38 (3)*, p. 515.

727 Crisp, D. (1986), Radiative forcing of the Venus mesosphere, *Icarus*, *67*, 484–514.

728 Crisp, D., and D. Titov (1997), The thermal balance of the Venus atmosphere, in *Venus II*,
729 *S.W. Bougher, D.M. Hunten, R.J. Phillips. The University of Arizona Press, Tucson*,
730 pp. 353–384.

731 de Bergh, C., V. I. Moroz, F. W. Taylor, D. Crisp, B. Bézard, and L. V. Zasova (2006),
732 The composition of the atmosphere of Venus below 100km altitude: An overview, *PSS*,

734 De Lataillade, A., J. L. Dufresne, M. El Hafi, V. Eymet, and R. Fournier (2002), A
735 net exchange Monte-Carlo approach to radiation in optically thick systems, *Journal of*
736 *Quantitative Spectroscopy and Radiative Transfer*, 74, 563–584.

737 Dufresne, J., C. Hourdin, R. Fournier, and F. Hourdin (2005), Net exchange reformula-
738 tion of radiative transfer in the CO_2 $15\mu m$ band on Mars, *Journal of the Atmospheric*
739 *Sciences*, 62, 3303–3319.

740 Dufresne, J. L., R. Fournier, and J. Y. Grandpeix (1998), Méthode de Monte-Carlo par
741 échanges pour le calcul des bilans radiatifs au sein d’une cavité 2D remplie de gaz,
742 *Compte-rendu de l’Académie des Sciences, Paris*, 326 Série II b, 33–38.

743 Esposito, L., R. Knollenberg, M. Marov, O. Toon, and R. Turco (1983), The clouds and
744 hazes of Venus, in *Venus*, D.M. Hunten, L. Colin, T.M. Donahue and V.I. Moroz. *The*
745 *University of Arizona Press, Tucson*, pp. 484–564.

746 Eymet, V., J. Dufresne, P. Ricchiazzi, R. Fournier, and S. Blanco (2004), Longwave
747 radiative analysis of cloudy scattering atmospheres using a net exchange formulation,
748 *Atmospheric Research*, 72, 238–261.

749 Eymet, V., J. Dufresne, R. Fournier, and S. Blanco (2005), A boundary-based net ex-
750 change Monte-Carlo Method for absorbing and scattering thick medium, *Journal of*
751 *Quantitative Spectroscopy and Radiative Transfer*, 95, 27–46.

752 Eymet, V., R. Fournier, S. Lebonnois, M. Bullock, J.-L. Dufresne, and F. Hourdin (2006),
753 An infrared radiative transfer parameterization for a Venus General Circulation Model,
754 in *DPS meeting, 2006, B.A.A.S. 38 (3)*, p. 527.

755 Fedorova, A., et al. (2008), HDO and H₂O vertical distributions and isotopic ratio in
756 the Venus mesosphere by solar occultation at infrared spectrometer on board Venus
757 Express, *JGR*, *113*, E00B22, doi:10.1029/2008JE003146.

758 Forget, F., F. Hourdin, R. Fournier, C. Hourdin, O. Talagrand, M. Collins, S. Lewis,
759 P. Read, and J. Huot (1999), Improved General Circulation Models of the Martian
760 atmosphere from the surface to above 80 km, *Journal of Geophysical Research*, *104*
761 *nE10*, 24,155–24,175.

762 Goody, R., and Y. Yung (1995), *Atmospheric radiation : Theoretical Basis*, Oxford Uni-
763 versity Press, Incorporated.

764 Goody, R., R. West, L. Chen, and D. Crisp (1989), The correlated-k method for radiation
765 calculations in nonhomogeneous atmospheres, *Journal of Quantitative Spectroscopy and*
766 *Radiative Transfer*, *42*, *n6*, 539–550.

767 Green, J. S. A. (1967), Division of radiative streams into internal transfer and cooling to
768 space, *Quarterly Journal of the Royal Meteorological Society*, *93*, 371–372.

769 Grinspoon, D., J. Pollack, B. Sitton, R. Carlson, L. Kamp, K. Baines, T. Encrenaz, and
770 F. Taylor (1993), Probing Venus’s cloud structure with Galileo NIMS, *Planetary Space*
771 *Science*, *41*, 515–542.

772 Gruszka, M., and A. Borysow (1997), Roto-translational collision-induced absorption of
773 CO₂ for the atmosphere of Venus at frequencies from 0 to 250 *cm*⁻¹ and at temperature
774 from 200k to 800k, *Icarus*, *129*, 172–177.

775 Hourdin, F., O. Talagrand, R. Sadourny, R. Courtin, D. Gautier, and C. McKay (1995),
776 General circulation of the atmosphere of Titan, *Icarus*, *117*, 358–374.

777 Hourdin, F., et al. (2006), The LMDZ4 General Circulation Model: climate performance
778 and sensitivity to parametrized physics with emphasis on tropical convection, *Climate*
779 *Dynamics*, *19*, 3445–3482.

780 Joseph, J., and R. Bursztyn (1976), A radiative cooling model in the thermal infrared
781 for application to models of the general circulation, *Journal of Applied Meteorology*, *15*,
782 319–325.

783 Knollenberg, R., and D. Hunten (1980), The microphysics of the clouds of Venus: re-
784 sults of the Pioneer Venus particle size spectrometer experiment, *Journal of Geophysical*
785 *Research*, *85*, 8039–8058.

786 Lacis, A. A., and J. E. Hansen (1991), Description of the correlated-k distribution method
787 for modeling nongray gaseous absorption, thermal emission, and multiple scattering
788 in vertically inhomogeneous atmospheres., *Journal of Geophysical Research*, *96*, 9027–
789 9063.

790 Lebonnois, S., F. Hourdin, V. Eymet, R. Fournier, and J.-L. Dufresne (2005), A new
791 Venus General Circulation Model, in the context of the Venus-Express mission, in *DPS*
792 *meeting, 2005. B.A.A.S. 37 (3)*, p. 742.

793 Lebonnois, S., A. Cresspin, F. Hourdin, V. Eymet, R. Fournier, and J.-L. Dufresne (2006),
794 Super-rotation simulated with the new LMD Venus General Circulation Model, in *EGU*
795 *General Assembly, 2006. Geophys. Res. Abstracts*, vol. 8, p. 06006, Vienna, Austria.

796 Moroz, V., A. Ekonomov, B. Moshkin, H. Revercomb, L. Sromovsky, J. Schofield,
797 D. Spänkuch, and M. Taylor, F.W. Tomasko (1985), Solar and thermal radiation in
798 the Venus atmosphere, *Adv. Space Res.*, *5(11)*, 197–232.

799 Moskalenko, N., Y. Il'in, S. Parzhin, and L. Rodionov (1979), Pressure-induced IR ra-
800 diation absorption in atmospheres, *Izvestiya, Atmospheric and Oceanic Physics*, *15*,
801 632–637.

802 Palmer, K., and D. Williams (1975), Optical constants of sulfuric acid: Application to
803 the clouds of Venus ?, *Applied Optics*, *14*, 208–219.

804 Perrin, M., and J. Hartmann (1989), Temperature-dependant measurements and modeling
805 of absorption by CO_2-N_2 mixtures in the far line-wings of the $4.3\mu m$ CO_2 band, *Journal*
806 *of Quantitative Spectroscopy and Radiative Transfer*, *42*, 311–317.

807 Pollack, J., D. Strecker, F. Witteborn, E. Erickson, and B. Baldwin (1978), Properties of
808 the clouds of Venus, as infered from airborne observations of its near infrared reflectivity
809 spectrum, *Icarus*, *34*, 28–45.

810 Pollack, J., O. Toon, and R. Boese (1980), Greenhouse models of Venus' high surface
811 temperature, as constrained by Pioneer Venus measurements, *Journal of Geophysical*
812 *Research*, *85*, 8223–8231.

813 Revercomb, H., L. Sromovsky, V. Suomi, and R. Boese (1985), Net thermal radiation in
814 the atmosphere of Venus, *Icarus*, *61*, 521–538.

815 Richardson, M. I., A. D. Toigo, and C. E. Newman (2007), PlanetWRF: A general purpose,
816 local to global numerical model for planetary atmospheric and climate dynamics, *J.*
817 *Geophys. Res.*, *112*(E9), E09001, doi:10.1029/2006JE002825.

818 Roberts, E., J. Selby, and L. Biberman (1976), Infrared continuum absorption by atmo-
819 spheric water vapor in the 8-12 μm window, *Appl. Opt.*, *15*, 2085–2090.

820 Roger, M. (2006), Modèles de sensibilité dans le cadre de la méthode de monte-carlo:
821 illustrations en transfert radiatif, Ph.D. thesis, Thèse de doctorat, Insitut National

823 Roger, M., S. Blanco, M. El Hafi, and R. Fournier (2005), Monte Carlo estimates of
824 domain-deformation sensitivities, *Physical Review Letters*, 95, number 18, 180,601–1 to
825 4.

826 Rothman, L., et al. (2000), HITEMP, the high-temperature molecular spectroscopic
827 database, available through <http://www.hitran.com>.

828 Rothman, L., et al. (2003), The HITRAN molecular spectroscopic database: Edition of
829 2000 including updates of 2001, *Journal of Quantitative Spectroscopy and Radiative*
830 *Transfer*, 82, 1–4.

831 Schubert, G. (1983), General circulation and the dynamical state of the Venus atmosphere,
832 in *Venus*, edited by D. M. Hunten, L. Colin, T. M. Donahue and V. I. Moroz, pp. 681–
833 765, Univ. of Arizona Press.

834 Seiff, A., et al. (1985), Models of the structure of the atmosphere of Venus from the surface
835 to 100 kilometers altitude, *Adv. Sp. Res.*, 5, 3–58.

836 Taylor, F., D. Crisp, and B. Bézard (1997), Near-infrared sounding of the lower atmo-
837 sphere of Venus, in *Venus II*, S.W. Bougher, D.M. Hunten, R.J. Phillips. *The University*
838 *of Arizona Press, Tucson*, pp. 325–351.

839 Titov, D. V., M. A. Bullock, D. Crisp, N. O. Renno, F. W. Taylor, and L. V. Zasova
840 (2007), Radiation in the atmosphere of Venus, in *Exploring Venus as a terrestrial planet*,
841 *Geophysical Monograph Series*, vol. 176, edited by L.W. Esposito, E.R. Stofan, and
842 Th.E. Cravens, pp. 121–138, American Geophysical Union.

843 Tomasko, M., L. Doose, P. Smith, and A. Odell (1980), Measurements of the flux of
844 sunlight in the atmosphere of Venus, *J. Geophys. Res.*, 85, 8167–8186.

845 Tomasko, M., L. Doose, and P. Smith (1985), The absorption of solar energy and the
 846 heating rate in the atmosphere of Venus, *Advances in Space Research*, 5, No.9, 71–79.
 847 vonZahn, U., and V. Moroz (1985), Composition of the Venus atmosphere below 100 km
 848 altitude, *Adv. Sp. Res.*, 5, 173–195.
 849 Washburn, E., C. West, and N. Dorsey (1930), *International Critical Tables of Numerical*
 850 *Data, Chemistry and Technology*, Mc Graw Hill, National Research Council, New York.
 851 Weise, K., and H. Zhang (1997), Uncertainty treatment in Monte-Carlo simulation, *Jour-*
 852 *nal of Physics A*, 30, 5971–5980.
 853 Zasova, L., N. Ignatiev, I. Khatuntsev, and V. Linkin (2007), Structure of the Venus
 854 atmosphere, *Planetary and Space Science*, 55, 1712–1728.

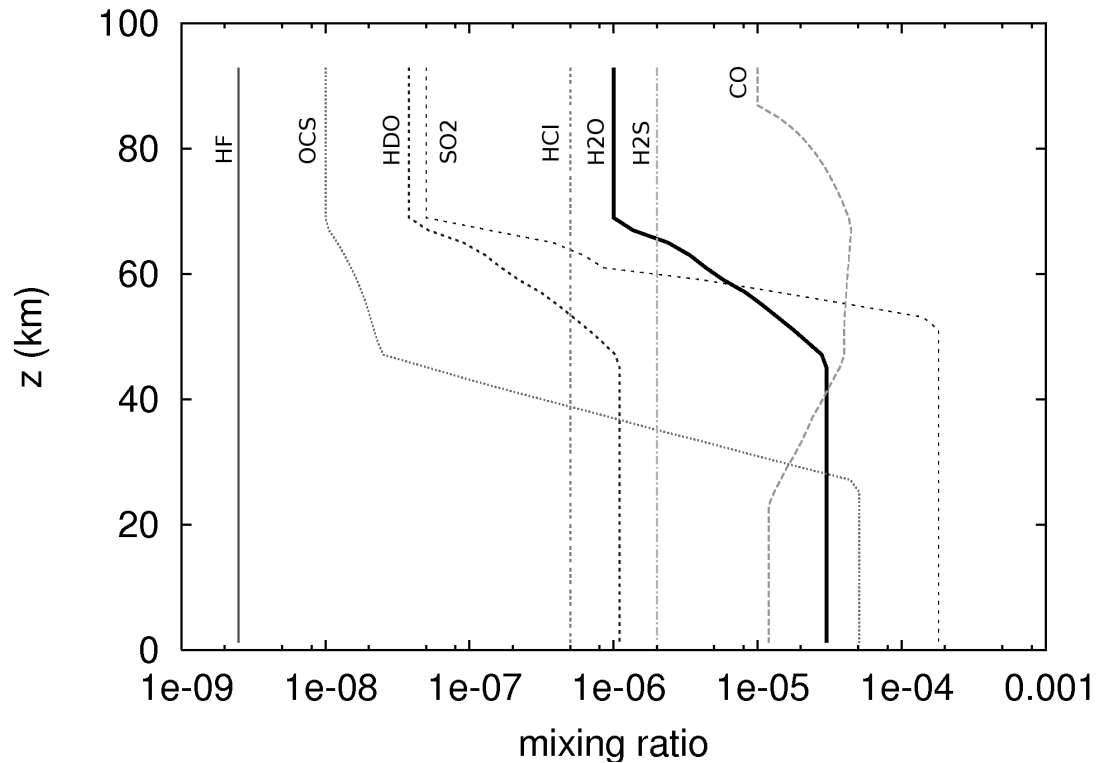


Figure 1. Mixing ratio of gaseous active species, as function of altitude (km).

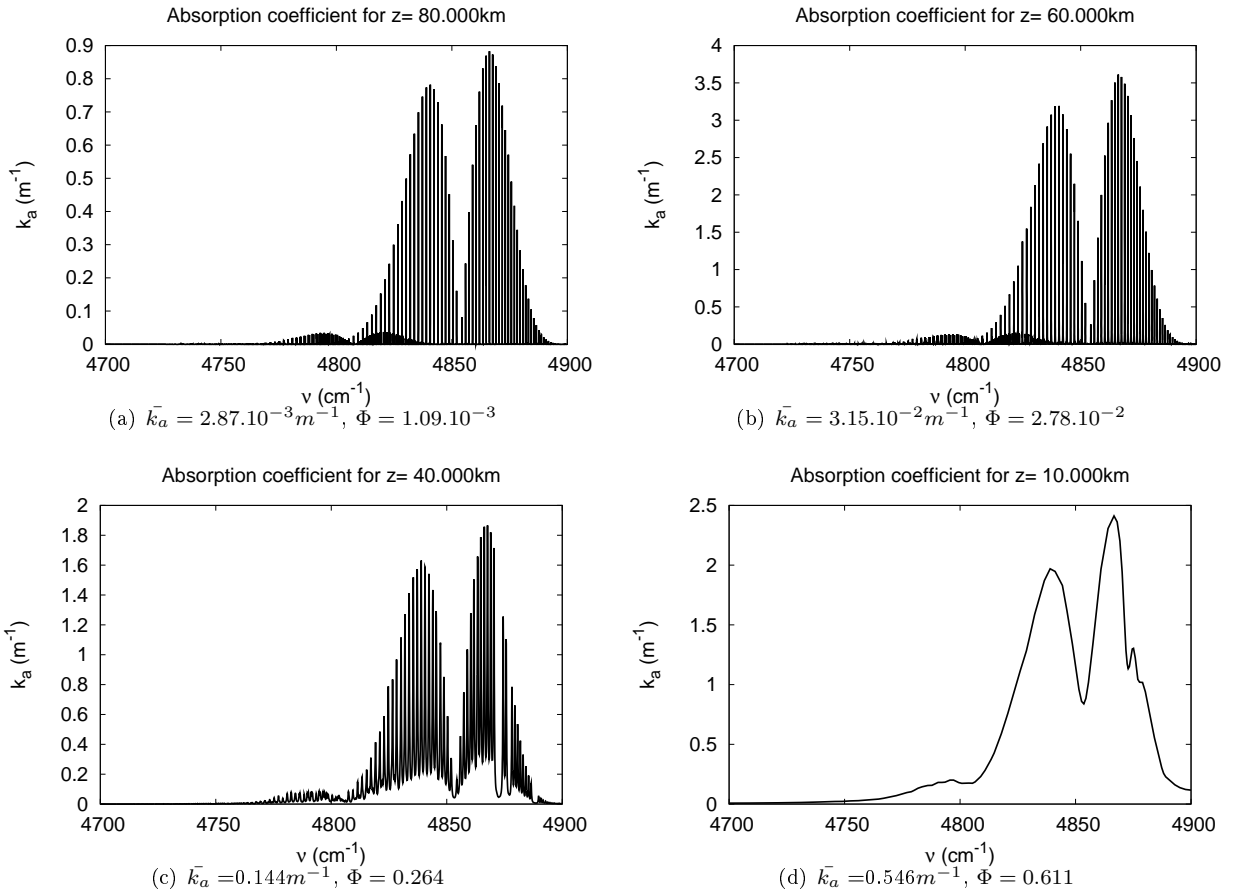


Figure 2. Absorption coefficient k_a (m^{-1}) as a function of wave number (cm^{-1}) in the [4700-4900] cm^{-1} (2.04-2.13 μm) spectral interval : at an altitude of (a) 80 km, (b) 60 km, (c) 40 km and (d) 10 km. The overlap parameter Φ and the average value \bar{k}_a of the absorption coefficient for this spectral interval are given underneath each figure.

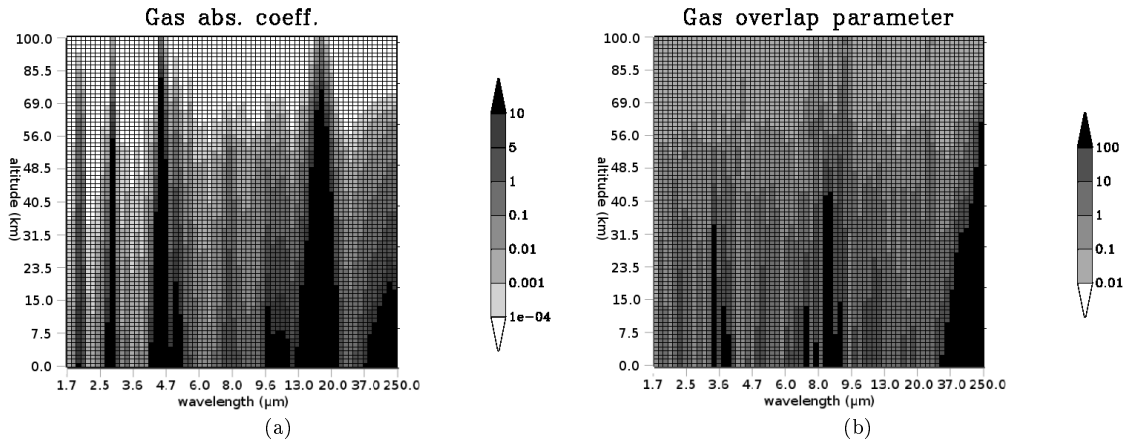


Figure 3. (a) T^{VIRA} average gaseous absorption coefficient \bar{k}_a (m^{-1}), as a function of wavelength and altitude. Including CO_2 collision-induced absorption. The spectral interval ranges from $1.71 \mu\text{m}$ to $250 \mu\text{m}$ ($40\text{-}5700 \text{ cm}^{-1}$) with a non-constant band width (Table 3). (b) Gas overlap parameter Φ .

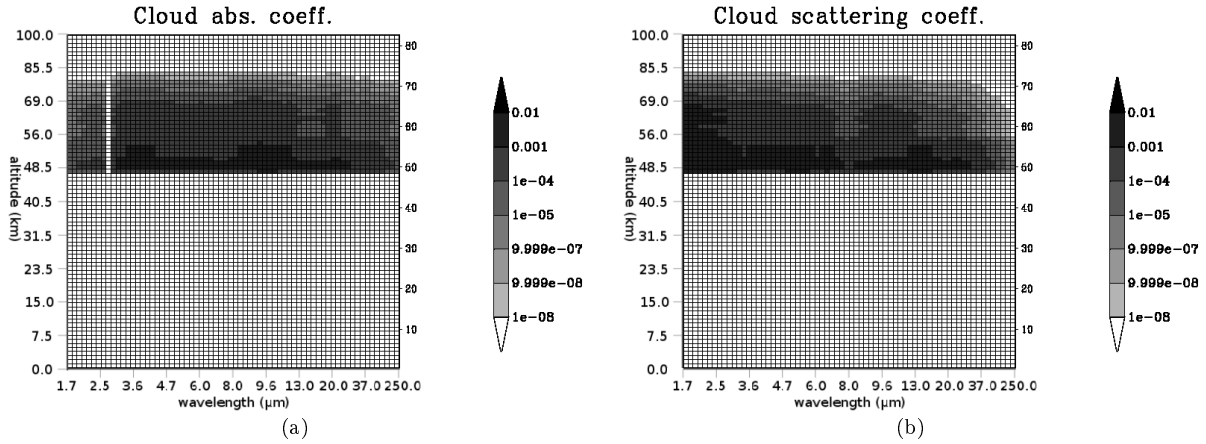


Figure 4. (a) Cloud absorption coefficient (in m^{-1}) and (b) cloud scattering coefficient (in m^{-1}), as function of wavelength and altitude .

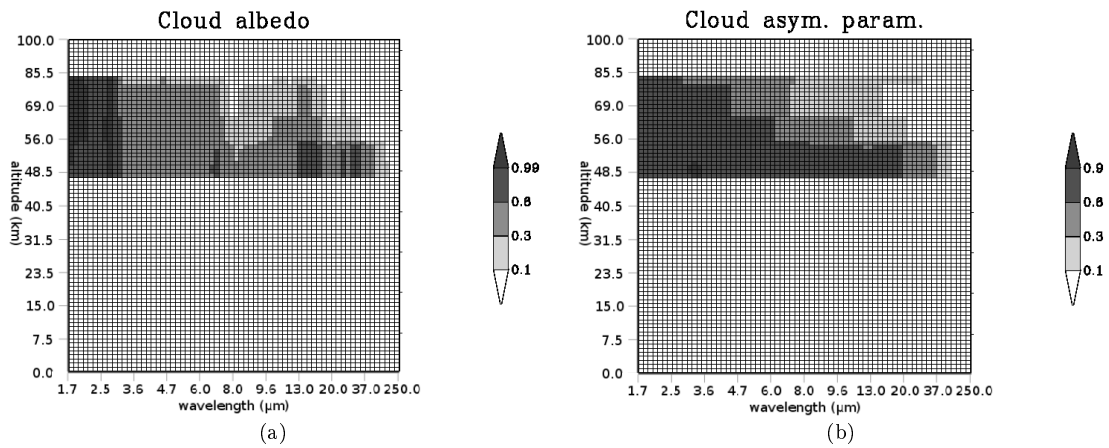


Figure 5. (a) Cloud single-scattering albedo and (b) cloud asymmetry parameter, as function of wavelength and altitude.

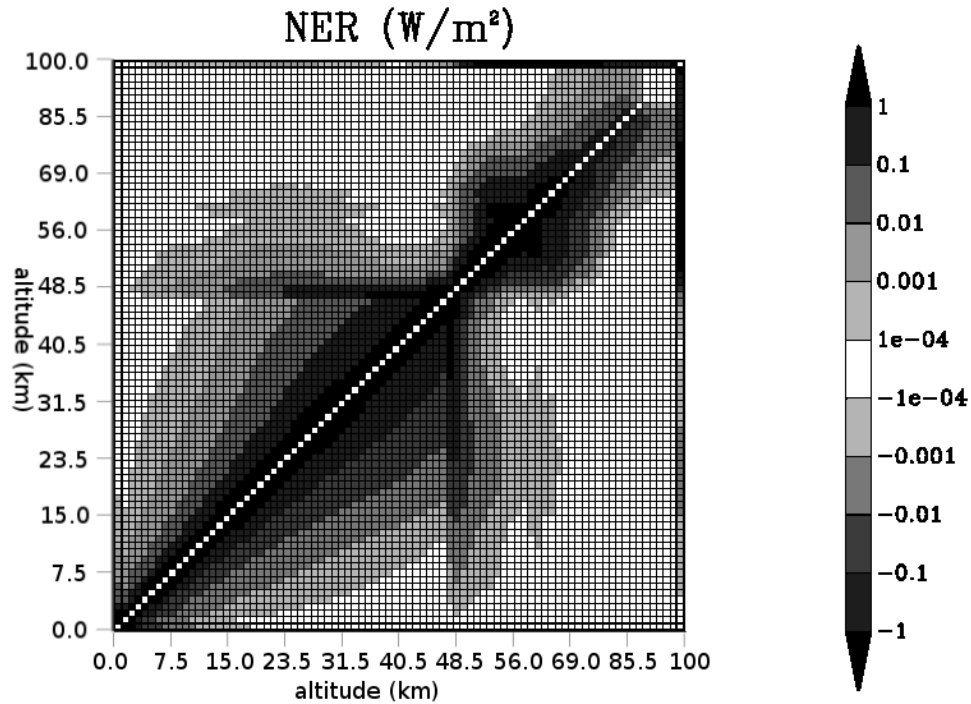


Figure 6. Spectrally integrated Net Exchange Rate matrix. The NER between atmospheric layers i and j is located at the intersection between row index i and column index j . The first row represents NERs between the ground and every atmospheric layer (ground heating). These NERs have a negative sign because the ground is cooled by radiative exchanges with the atmosphere. The last row represents NERs between all atmospheric layers and space (cooling to space). These NERs are positive because space is heated by radiative exchanges with the atmosphere.

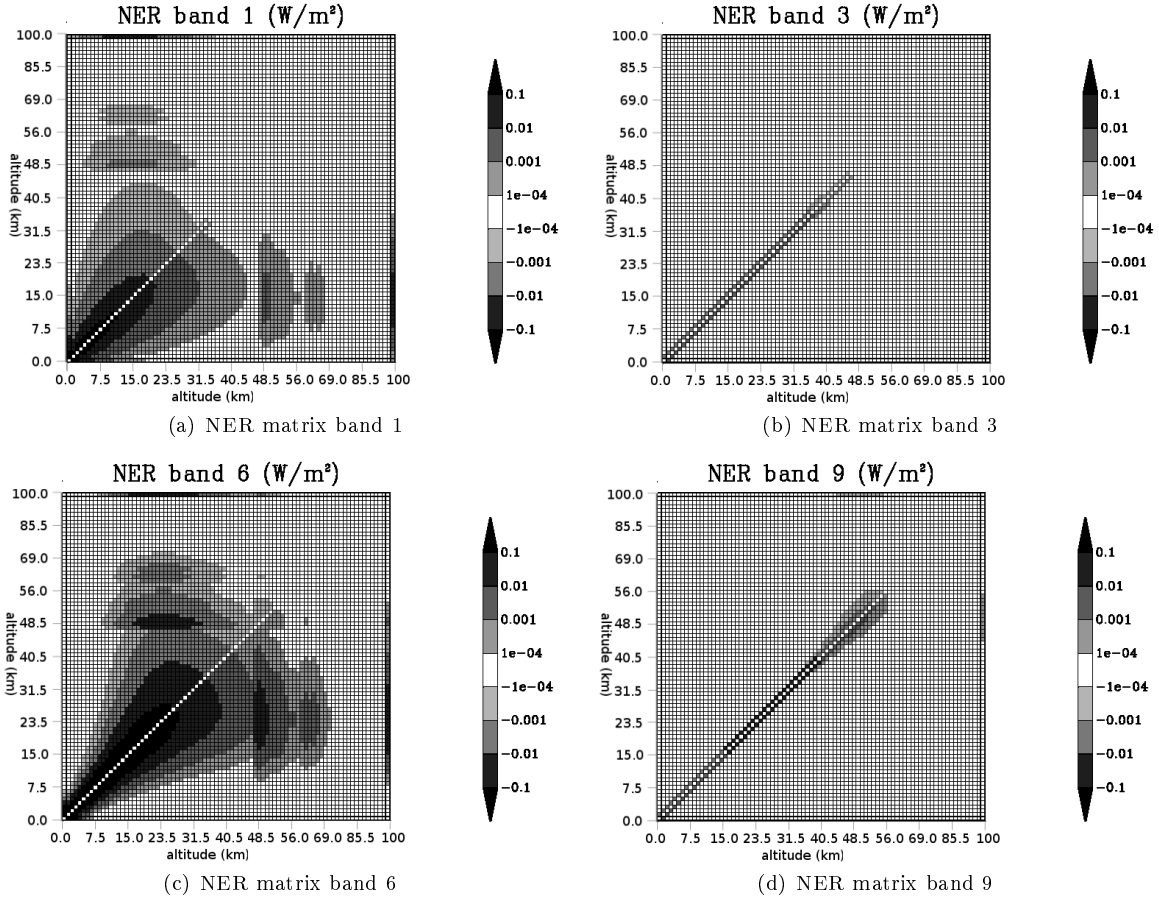


Figure 7. NER matrixes in selected narrow bands: (a) narrow band number 1, extending from 5700 cm^{-1} to 5825 cm^{-1} ($1.71\text{-}1.75\text{ }\mu\text{m}$). (b) narrow band number 3, $4950\text{-}5200\text{ cm}^{-1}$ ($1.92\text{-}2.02\text{ }\mu\text{m}$). (c) narrow band number 6, $4134\text{-}4350\text{ cm}^{-1}$ ($2.30\text{-}2.42\text{ }\mu\text{m}$). (d) narrow band number 9, $3760\text{-}3875\text{ cm}^{-1}$ ($2.58\text{-}2.66\text{ }\mu\text{m}$).

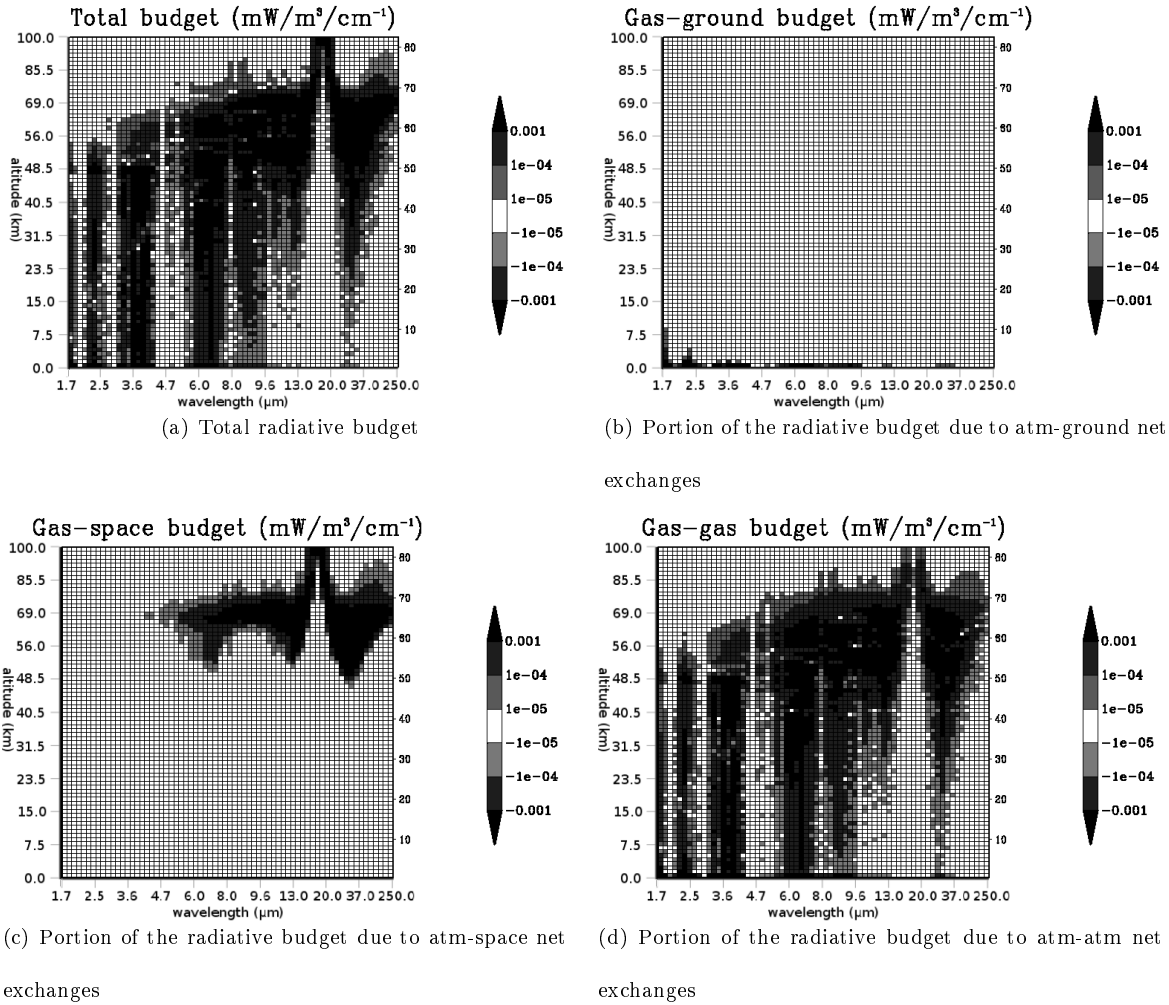


Figure 8. (a) Total radiative budget per cubic meter ($\zeta_{nb}(i)/\Delta z_i$, where Δz_i is the thickness of layer i), as a function of wavelength and altitude. This total radiative budget is then decomposed in (b) net exchanges with the ground, (c) net exchanges with space and (d) net exchanges between atmospheric layers.

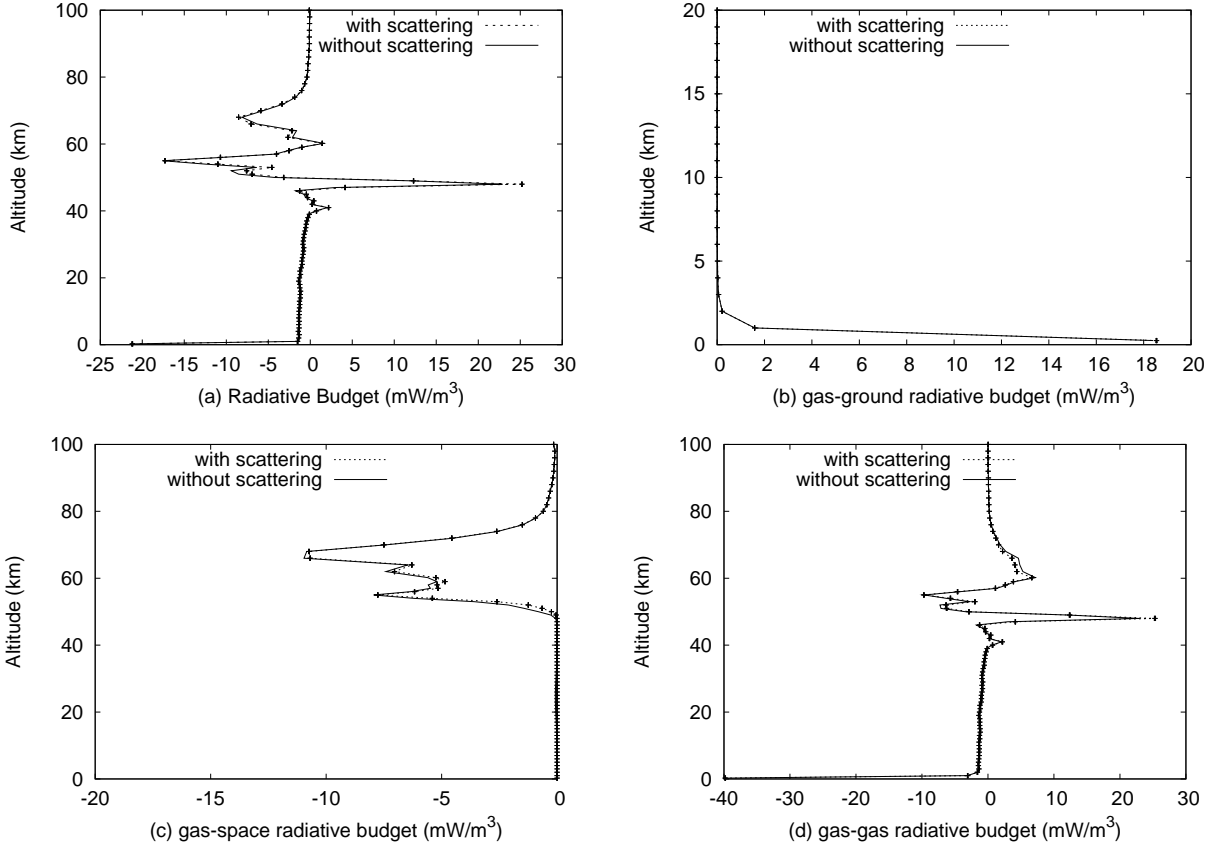


Figure 9. Spectrally integrated radiative budget in mW/m^3 ($\zeta_{nb}(i)/\Delta z_i$, where Δz_i is the thickness of layer i) computed with and without scattering. The total radiative budget (a) is decomposed in (b) portion of the budget due to exchanges with the ground, (c) portion of the budget due to exchanges with space and (d) portion of the budget due to exchanges between atmospheric layers.

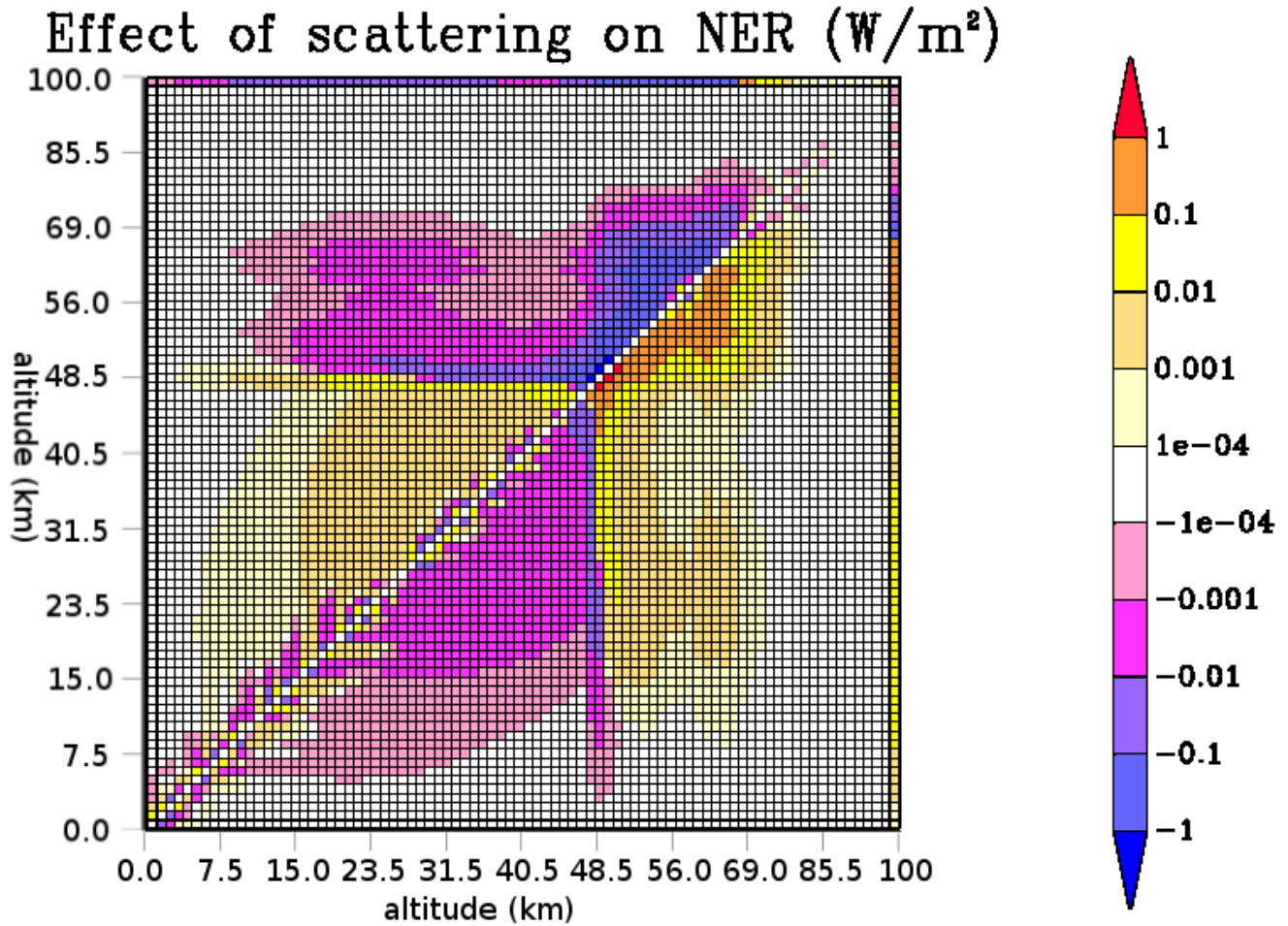


Figure 10. Spectrally integrated matrix of the effect of scattering on Net Exchange Rates. This figure represents $d\Psi(i, j) = \Psi(i, j) - \Psi^{aa}(i, j)$, with $\Psi(i, j)$ the reference spectrally integrated NER between layers i and j , and $\Psi^{aa}(i, j)$ the spectrally integrated NER between layers i and j , computed within the absorption approximation (analytical result in a scattering-free atmosphere).

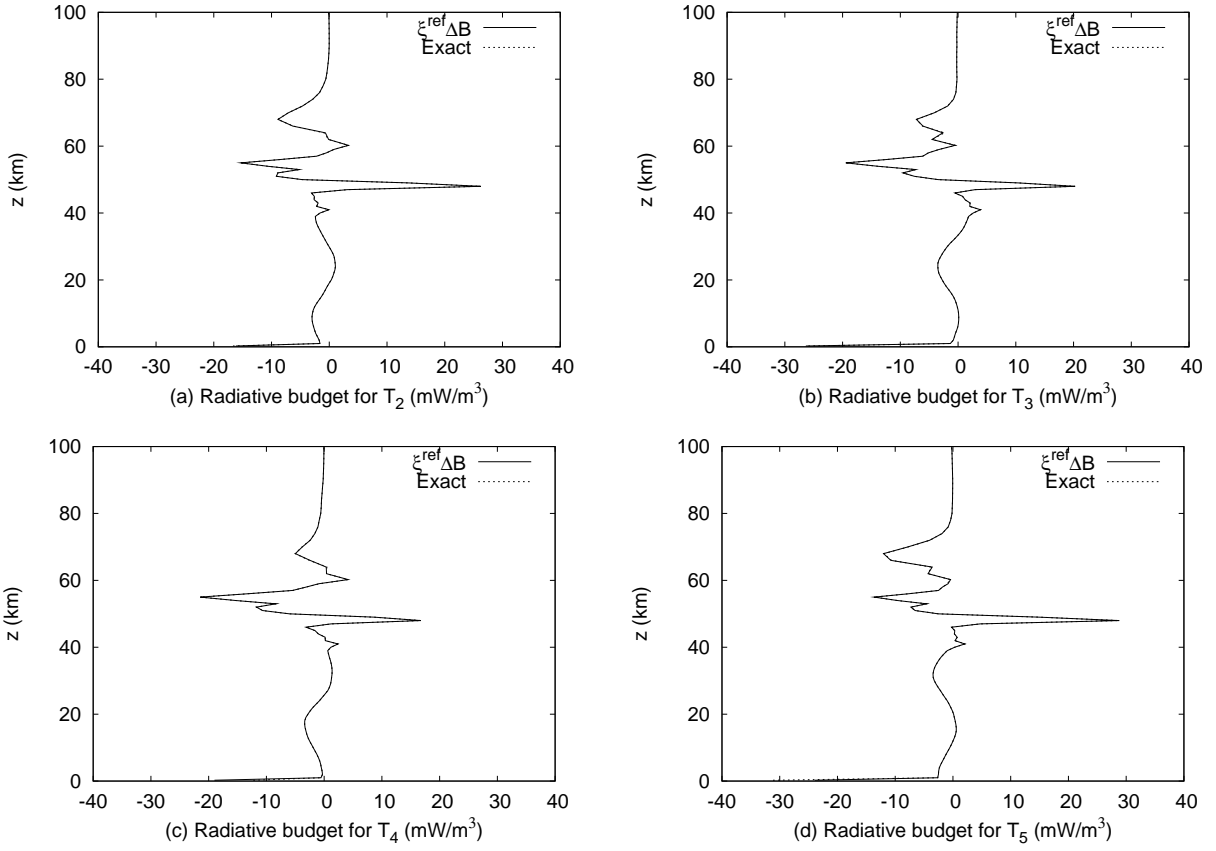


Figure 11. Radiative budget (mW/m^3) as function of altitude, $(\zeta_{nb}(i)/\Delta z_i)$, where Δz_i is the thickness of layer i) for the four test temperature profiles T_2 to T_5 , fixing the absorption properties to those of the reference temperature profile $T_1 = T^{VIRA}$. The results labeled $\xi^{ref} \Delta B$ correspond to those of the proposed parameterization with a constant ξ^{ref} computed for $T_1 = T^{VIRA}$.

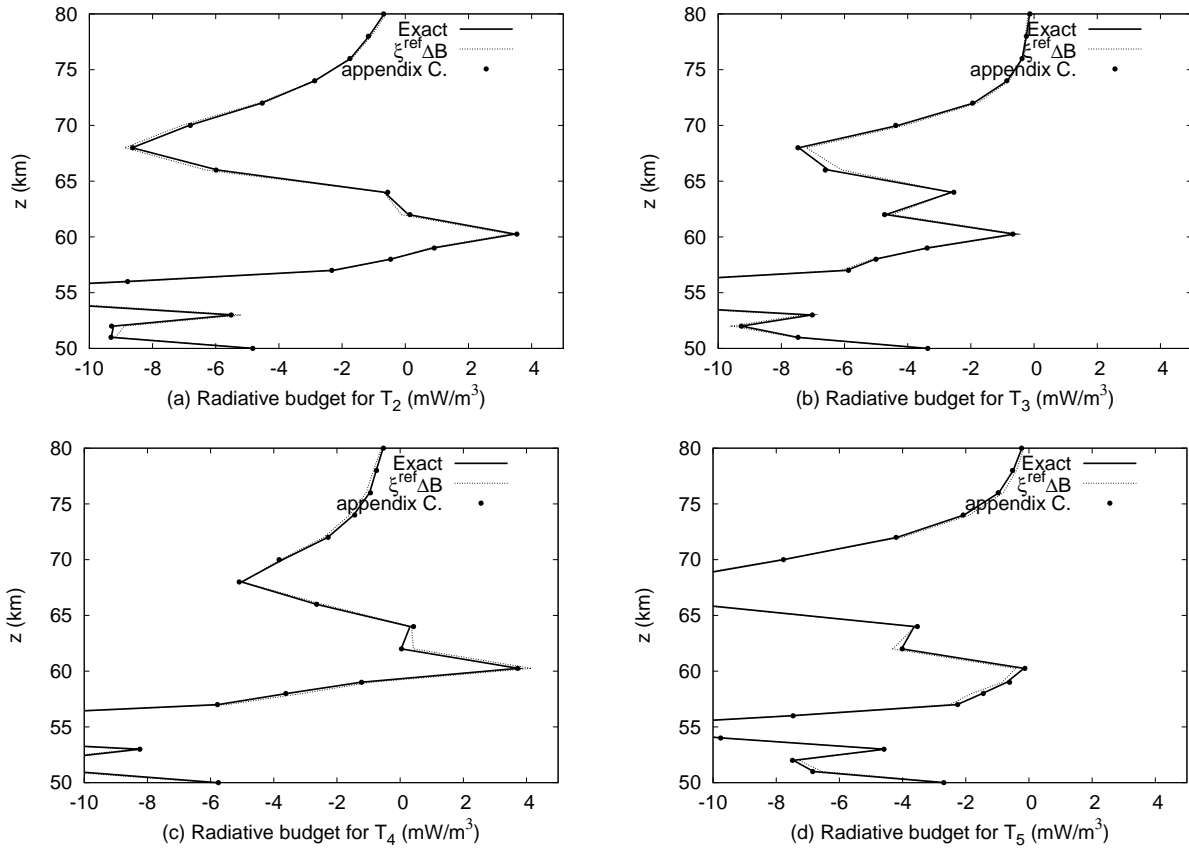


Figure 12. Same as Fig. 11 above 50km, with absorption properties function of temperature, (for the exact solution, the k-distribution data have been interpolated using the $T^{VIRA} - 10K$, T^{VIRA} and $T^{VIRA} + 10K$). Also displayed, the results of the upgraded parameterization described in appendix C.

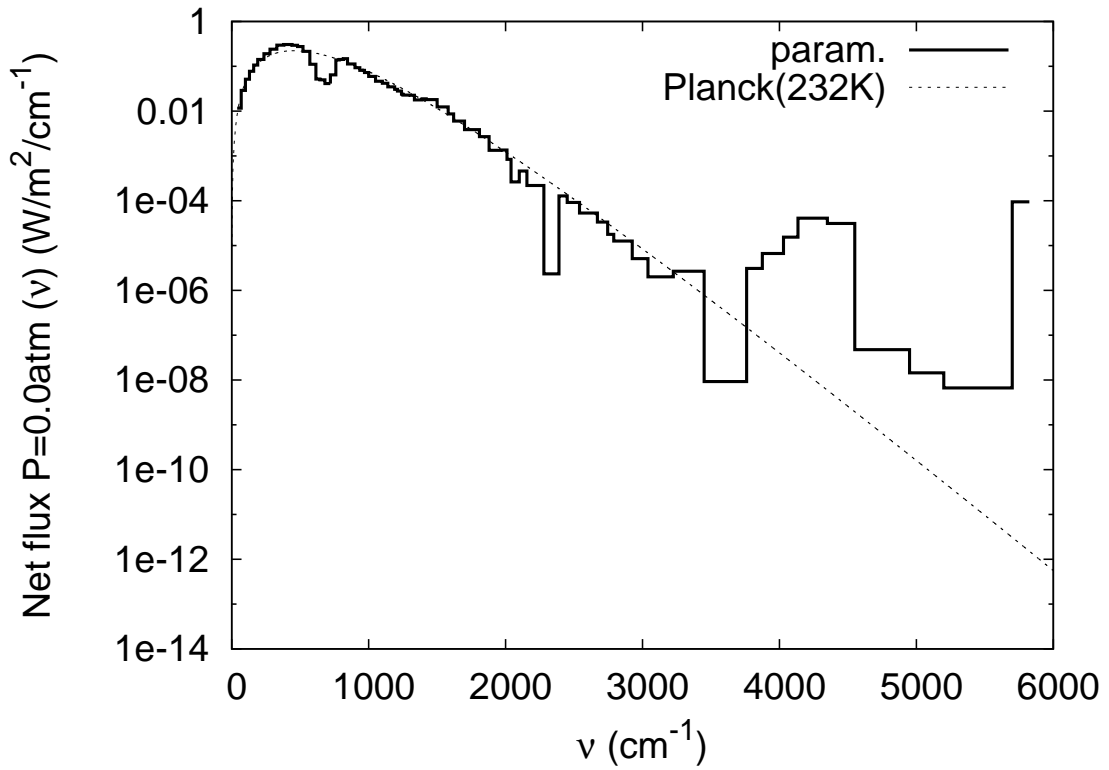


Figure 13. Net flux signal in $W/m^2/cm^{-1}$ at the top of atmosphere ($P=0.0atm$) in the $[0-6000]$ cm^{-1} spectral range. Net flux at the top of atmosphere is compared to the Planck intensity at 232K using a logscale.

Table 1. Nominal cloud model data, originally taken from *Zasova et al.* [2007]. The size distribution of each particle mode is described by a log-normal distribution of modal radius \bar{r} , logarithmic width σ_{log} (see Appendix B) and a mass percentage of sulfuric acid.

	Mode 1	Mode 2	Mode 2'	Mode 3
\bar{r} (μm)	0.15	1.05	1.40	3.85
σ_{log}	1.91	1.21	1.23	1.30
H ₂ SO ₄ mass %	84.5	84.5	84.5	84.5

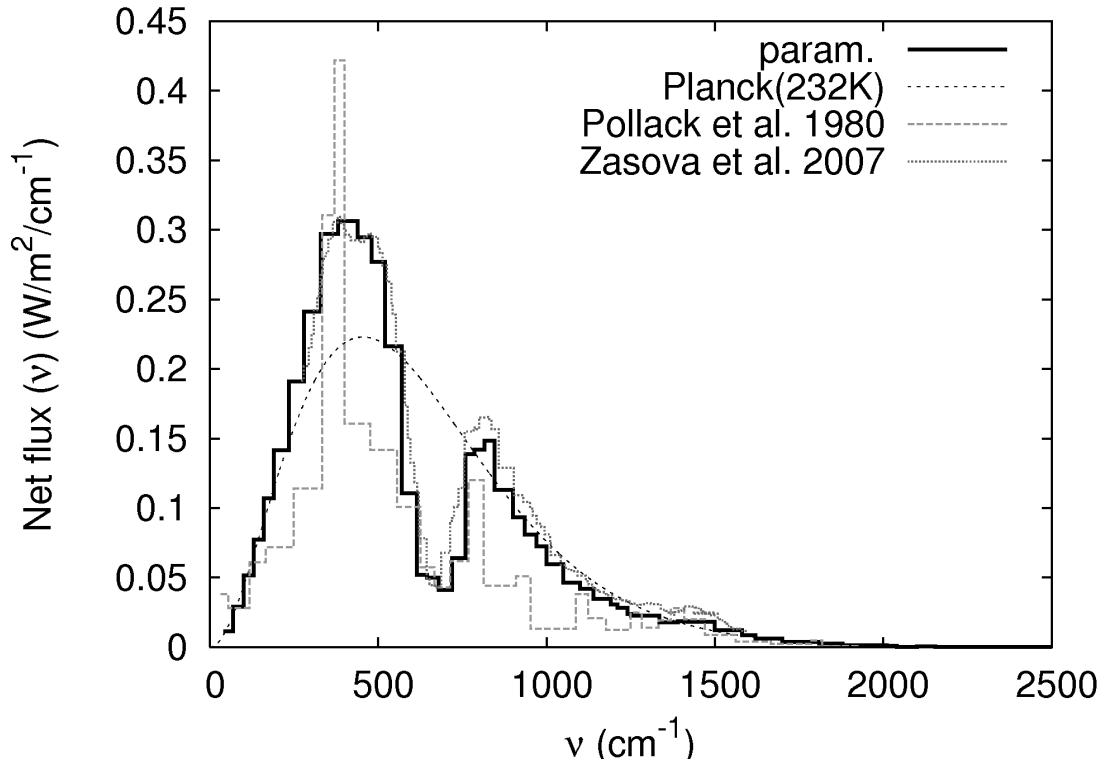


Figure 14. Net flux signal in $W/m^2/cm^{-1}$ at the top of atmosphere ($P=0.0\text{atm}$) in the $[0-2500] \text{ cm}^{-1}$ spectral range. Reference results are compared to the Planck intensity at 232K, computational results from *Pollack et al.* [1980], and observational results from *Zasova et al.* [2007].

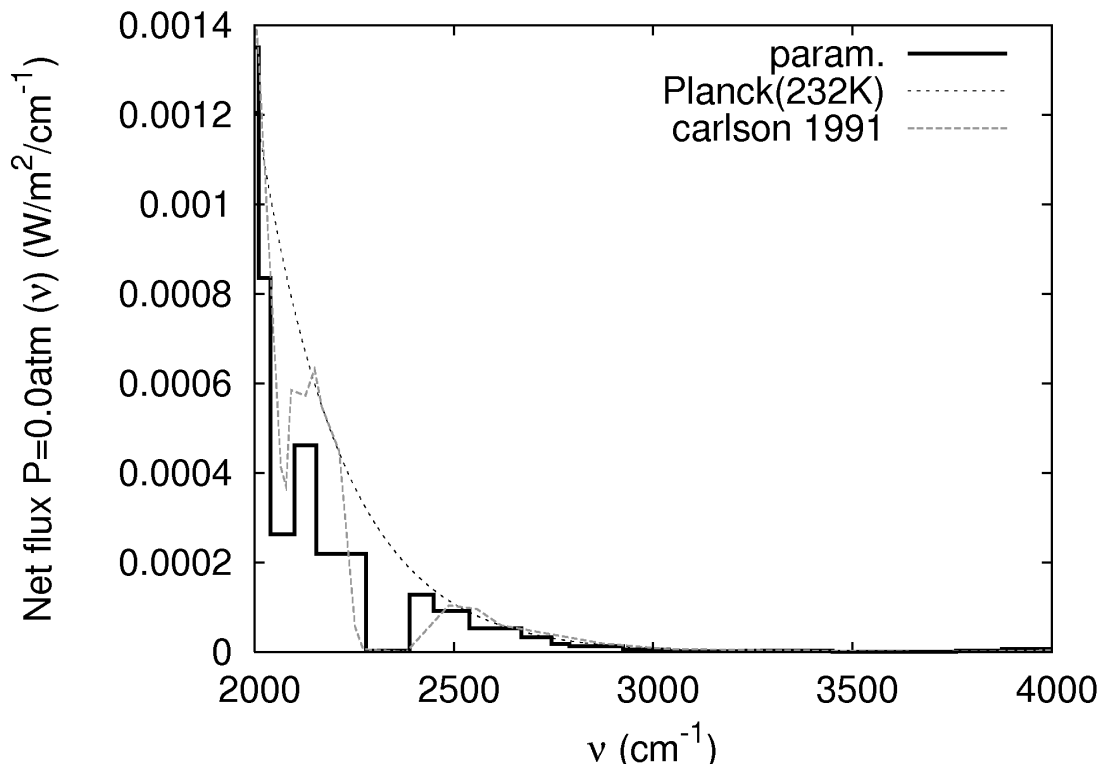


Figure 15. Net flux signal in $W/m^2/cm^{-1}$ at the top of atmosphere ($P=0.0\text{atm}$) in the $[2000-4000]$ cm^{-1} spectral range. Net flux at the top of atmosphere is compared to the Planck intensity at 232K, and observational results from *Carlson* [1991].

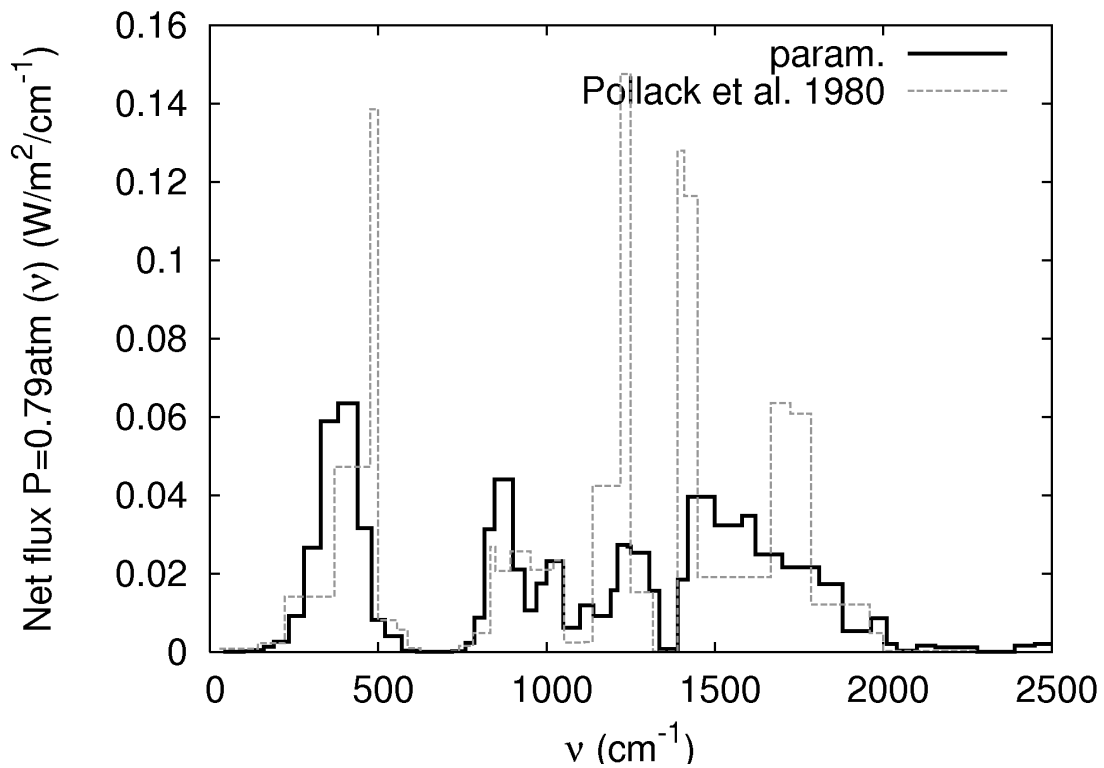


Figure 16. Net flux signal in $\text{W}/\text{m}^2/\text{cm}^{-1}$ at a pressure of 0.79atm (around 53km altitude) in the $[0\text{-}2500]$ cm^{-1} spectral range. Simulation results are compared to the computational result of *Pollack et al.* [1980].

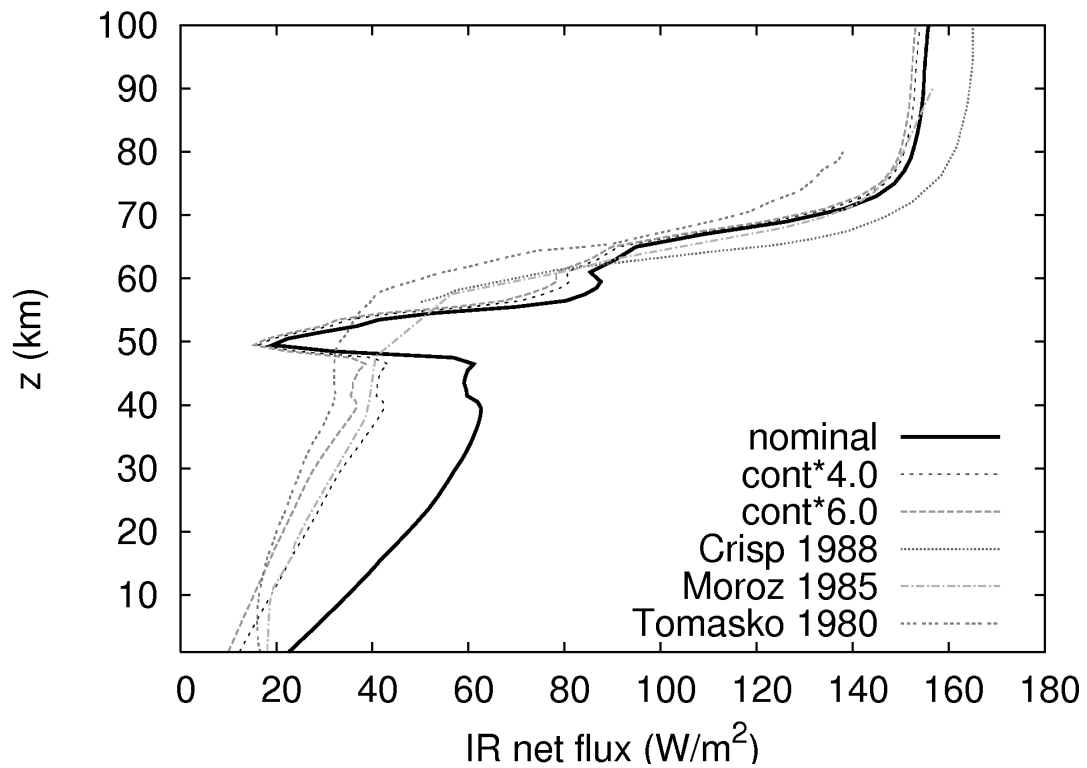


Figure 17. Net flux in W/m^2 as function of altitude for our nominal model and for continuum optical depth increased by factors 4 and 6. Solar net flux profiles from *Crisp* [1986], *Moroz et al.* [1985] and *Tomasko et al.* [1980] are also displayed.

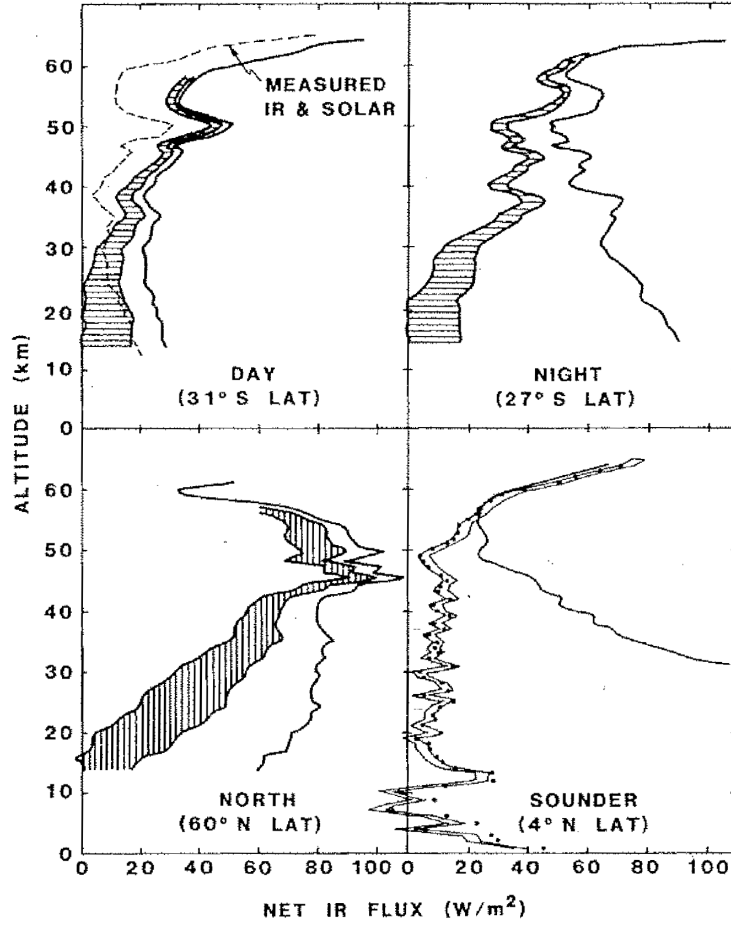


Figure 18. Thermal net flux profiles (W/m^2) from *Revercomb et al.* [1985].

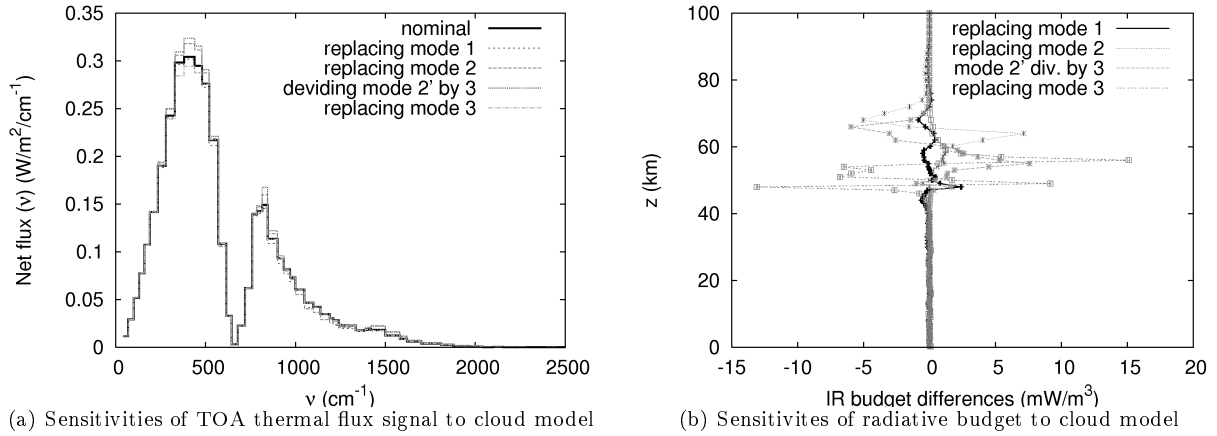


Figure 19. Sensitivities of top of atmosphere flux signal (a) and radiative budget (b) to cloud model. Nominal modal radiuses and standard deviations, as well as particles concentration from *Zasova et al.* [2007] for modes 1, 2 and 3 have been replaced by data from *Knollenberg and Huntten* [1980]. Nominal particles concentration for mode 2' have been divided by a factor 3.

Table 2. Nominal particle densities (cm^{-3}) used in the log-normal size distribution of cloud droplets. Nominal particle densities are defined for 36 layers. Layer i extends from $z_{min}(i)$ to $z_{max}(i)$ (for each particle mode). See Appendix B for a description of the log-normal distribution.

$z_{max}(i)$ (km)	$z_{min}(i)$ (km)	$N_0(1)(i)$	$N_0(2)(i)$	$N_0(2')(i)$	$N_0(3)(i)$
84.000	83.000	1.	0.	0.	0.
83.000	82.000	2.	0.	0.	0.
82.000	81.000	4.	0.	0.	0.
81.000	80.000	6.	0.	0.	0.
80.000	79.000	10.	1.	0.	0.
79.000	78.000	15.	1.	0.	0.
78.000	77.000	20.	2.	0.	0.
77.000	76.000	30.	3.	0.	0.
76.000	75.000	50.	5.	0.	0.
75.000	74.000	70.	7.	0.	0.
74.000	73.000	110.	11.	0.	0.
73.000	72.000	160.	16.	0.	0.
72.000	71.000	240.	24.	0.	0.
71.000	70.000	360.	36.	0.	0.
70.000	69.000	530.	53.	0.	0.
69.000	68.000	800.	80.	0.	0.
68.000	67.000	1200.	120.	0.	0.
67.000	66.000	1800.	180.	0.	0.
66.000	65.000	1500.	150.	0.	0.
65.000	64.000	200.	0.	20.	0.
64.000	63.000	750.	0.	75.	0.
63.000	62.000	750.	0.	75.	0.
62.000	61.000	750.	0.	75.	0.
61.000	60.000	750.	0.	75.	0.
60.000	59.000	500.	0.	30.	0.
59.000	58.000	500.	0.	50.	0.
58.000	57.000	500.	0.	50.	0.
57.000	56.000	300.	0.	50.	0.
56.000	55.000	500.	0.	50.	3.
55.000	54.000	500.	0.	50.	10.
54.000	53.000	500.	0.	50.	10.
53.000	52.000	500.	0.	50.	10.
52.000	51.000	500.	0.	50.	10.
51.000	50.000	500.	0.	50.	20.
50.000	49.000	500.	0.	50.	30.
49.000	48.000	500.	0.	50.	20.

Appendix A: Spectral mesh

Table 3. Spectral limits of the 68 narrow bands.

Band index	Lower λ (μm)	Upper λ (μm)	Lower ν (cm^{-1})	Upper ν (cm^{-1})
1	1.717	1.755	5699.62	5825.00
2	1.755	1.923	5200.12	5699.62
3	1.923	2.020	4950.37	5200.12
4	2.020	2.198	4549.75	4950.37
5	2.198	2.299	4349.95	4549.75
6	2.299	2.418	4134.86	4349.95
7	2.418	2.481	4029.87	4134.86
8	2.481	2.581	3874.92	4029.87
9	2.581	2.660	3759.73	3874.92
10	2.660	2.899	3449.84	3759.73
11	2.899	3.101	3224.55	3449.84
12	3.101	3.289	3040.04	3224.55
13	3.289	3.419	2924.85	3040.04
14	3.419	3.584	2790.30	2924.85
15	3.584	3.642	2745.44	2790.30
16	3.642	3.745	2670.01	2745.44
17	3.745	3.938	2539.53	2670.01
18	3.938	4.082	2449.82	2539.53
19	4.082	4.185	2389.68	2449.82
20	4.185	4.387	2279.58	2389.68
21	4.387	4.640	2155.22	2279.58
22	4.640	4.762	2100.17	2155.22
23	4.762	4.902	2040.03	2100.17
24	4.902	4.974	2010.47	2040.03
25	4.974	5.090	1964.60	2010.47
26	5.090	5.319	1879.99	1964.60
27	5.319	5.526	1809.65	1879.99
28	5.526	5.884	1699.56	1809.65
29	5.884	6.173	1620.04	1699.56
30	6.173	6.328	1580.29	1620.04
31	6.328	6.668	1499.76	1580.29
32	6.668	7.041	1420.24	1499.76
33	7.041	7.196	1389.66	1420.24
34	7.196	7.493	1334.62	1389.66
35	7.493	7.663	1305.05	1334.62
36	7.663	8.000	1250.01	1305.05
37	8.000	8.066	1239.81	1250.01
38	8.066	8.263	1210.25	1239.81
39	8.263	8.404	1189.86	1210.25
40	8.404	8.773	1139.91	1189.86
41	8.773	9.090	1100.16	1139.91
42	9.090	9.522	1050.21	1100.16
43	9.522	9.997	1000.26	1050.21
44	9.997	10.31	969.677	1000.26
45	10.31	10.69	935.018	969.677
46	10.69	11.11	900.359	935.018
47	11.11	11.83	845.313	900.359
48	11.83	12.27	814.731	845.313
49	12.27	12.74	785.169	814.731
50	12.74	13.16	759.685	785.169
51	13.16	13.89	719.929	759.685
52	13.89	14.70	680.173	719.929
53	14.70	15.52	644.494	680.173
54	15.52	16.26	614.932	644.494
55	16.26	17.54	570.079	614.932
56	17.54	19.23	520.130	570.079
57	19.23	20.82	480.374	520.130
58	20.82	22.75	439.598	480.374
59	22.75	26.28	380.474	439.598
60	26.28	30.35	329.505	380.474
61	30.35	35.77	279.555	329.505
62	35.77	42.61	234.702	279.555
63	42.61	52.67	189.849	234.702
64	52.67	62.39	160.287	189.849
65	62.39	77.10	129.706	160.287
66	77.10	99.86	100.144	129.706
67	99.86	143.8	69.5621	100.144
68	143.8	250.0	40.0000	69.5621

Appendix B: Clouds optical properties

855 The log-normal distribution used for describing cloud droplets size distributions in this article
856 is $n(r) = N_0 p(r)$, where N_0 is the nominal particle density and the probability density function
857 p is defined as

$$p(r) = \frac{1}{\sqrt{2\pi} \cdot r \cdot \sigma_{log}} \exp\left[-\frac{1}{2} \left(\frac{\ln(\frac{r}{\bar{r}})}{\sigma_{log}}\right)^2\right] \quad (\text{B1})$$

858 where \bar{r} is the modal radius and σ_{log} is the logarithmic width. The effective radius r_e is defined
859 as: $r_e = \frac{\langle r^3 \rangle}{\langle r^2 \rangle}$, with:

$$\langle r^2 \rangle = \int_0^{+\infty} p(r) r^2 dr = \bar{r}^2 \exp\left(2 \ln(\sigma)^2\right) \quad (\text{B2})$$

$$\langle r^3 \rangle = \int_0^{+\infty} p(r) r^3 dr = \bar{r}^3 \exp\left(\frac{9}{2} \ln(\sigma)^2\right) \quad (\text{B3})$$

860 leading to:

$$r_e = \bar{r} \cdot \exp\left(\frac{5}{2} \ln(\sigma)^2\right) \quad (\text{B4})$$

861 A program based on the Mie scattering theory is used in order to compute extinction efficiency
862 factors q_{ext} , single-scattering albedos ω and asymmetry parameters g as functions of wavenumber,
863 for each particle mode. The microphysical parameters are:

- 864 • the log-normal distribution parameters for each particle mode, from *Knollenberg and Hunten*
865 [1980] and *Grinspoon et al.* [1993] (see Tables 1 and 2).
- 866 • the mass percentage of H_2SO_4 for each particle mode [*Knollenberg and Hunten*, 1980] (see
867 Table 1).

868 • the complex refractive index of H_2SO_4 solutions, as function of wavenumber, from *Palmer*
 869 *and Williams* [1975].

870 The extinction optical depth τ_{ext} of a given atmospheric layer, for a given particle mode, is:

$$\tau_{ext} = \frac{3 q_{ext} \cdot M}{4 \rho \cdot r_e} \quad (\text{B5})$$

871 where ρ is the particle volumic mass and M is the surfacic mass corresponding to the particles in
 872 the considered layer (that extends from z_1 to z_2), that can be computed as $M(z_1, z_2) = \rho \frac{4}{3} \pi <$
 873 $r^3 > \int_{z_1}^{z_2} N_0(z) dz$, which leads to $\tau_{ext} = \pi q_{ext} \bar{r}^2 \exp(2 \ln^2(\sigma)) \int_{z_1}^{z_2} N_0(z) dz$.

874 The absorption τ_a and scattering τ_s optical depths for the considered particle mode are $\tau_s =$
 875 $\tau_{ext} \omega$ and $\tau_a = (1 - \omega) \tau_{ext}$. Total optical depths for each layer are the sum of the contributions
 876 of all particle modes.

Appendix C: Simple upgrades for the upper atmosphere

877 Upgrading the parameterization in order to include opacity variations with temperature is
 878 widely simplified by the fact that scattering has only a little influence on infrared radiative
 879 transfers above the clouds (Fig. 9 and 10). All NERs involving atmospheric layers above the
 880 clouds can be accurately modeled under the absorption approximation. This means that the
 881 analytical form of each $\bar{\xi}_{nb}(i, j)$ can be partially derived as function of each temperature \bar{T}_p to
 882 produce analytical expressions of the sensitivities $\frac{\partial \bar{\xi}_{nb}^{ref}(i, j)}{\partial \bar{T}_p}$ around T^{VIRA} for each layer index p
 883 between i and j . A linear expansion of $\bar{\xi}_{nb}(i, j)$ can then be used to derive the following upgraded
 884 version of the parameterization :

$$\Psi_{nb}(i, j) \approx \left[\bar{\xi}_b^{ref}(i, j) + \sum_{p=\min(i, j)}^{\max(i, j)} \frac{\partial \bar{\xi}_{nb}^{ref}(i, j)}{\partial \bar{T}_p} (\bar{T}_p - \bar{T}_p^{ref}) \right] (B_{nb}(j) - B_{nb}(i)) \quad (\text{C1})$$

885 Before any accuracy test, we first checked that the linear expansion induces no violation of
886 the reciprocity principle, meaning that whatever the non-linearities of $\bar{\xi}_{nb}(i, j)$ with temperature
887 (opacities are linearly interpolated but extinctions are exponential) $\bar{\xi}_{nb}^{ref}(i, j) + \sum_p \frac{\partial \bar{\xi}_{nb}^{ref}(i, j)}{\partial \bar{T}_p} (\bar{T}_p -$
888 $\bar{T}_p^{ref})$ remains positive for all i, j and nb in the considered perturbation range. For the four
889 sinusoidal perturbations described above, no such difficulty was encountered. Results in terms of
890 cooling rates indicate that the opacity variations are well reproduced with such a parameterization
891 (not shown).

892 However, the partial derivatives $\frac{\partial \bar{\xi}_{nb}^{ref}(i, j)}{\partial \bar{T}_p}$ require a much larger storage than $\bar{\xi}_{nb}^{ref}(i, j)$ which is a
893 severe handicap. A first practical solution is to make use of Eq. C1 only for the dominant NERs
894 (NERs with space, with the two adjacent layers, and with one or two layers at the top of the
895 cloud) and to keep the standard parameterization for the remaining NERs. But this still leads
896 to a factor 4 or a factor 5 increase of the storage requirement. This can be reduced by linearizing
897 the Planck function for the correction term :

$$\begin{aligned} \Psi_{nb}(i, j) &\approx \bar{\xi}_{nb}^{ref}(i, j)(B_{nb}(j) - B_{nb}(i)) + \left[\sum_{p=0}^{m+1} \frac{\partial \bar{\xi}_{nb}^{ref}(i, j)}{\partial \bar{T}_p} (\bar{T}_p - \bar{T}_p^{ref}) \right] \\ &* \left[B_{nb}^{ref}(j) + \frac{\partial B_{nb}^{ref}(j)}{\partial \bar{T}_j} (\bar{T}_j - \bar{T}_j^{ref}) - B_{nb}^{ref}(i) - \frac{\partial B_{nb}^{ref}(i)}{\partial \bar{T}_i} (\bar{T}_i - \bar{T}_i^{ref}) \right] \end{aligned}$$

898 This allows to sum once over the narrow-bands before applying the perturbation :

$$\begin{aligned} \Psi(i, j) &= \sum_{nb=1}^{N_b} \Psi_{nb}(i, j) \\ &\approx \sum_{nb=1}^{N_b} \bar{\xi}_{nb}^{ref}(i, j)(B_{nb}(j) - B_{nb}(i)) \\ &+ \sum_{p=0}^{m+1} (\bar{T}_p - \bar{T}_p^{ref}) \left[A_{i,j,p}^{ref} + C_{i,j,p}^{ref} (\bar{T}_j - \bar{T}_j^{ref}) - D_{i,j,p}^{ref} - E_{i,j,p}^{ref} (\bar{T}_i - \bar{T}_i^{ref}) \right] \end{aligned}$$

$$A_{i,j,p}^{ref} = \sum_{nb=1}^{N_b} \frac{\partial \bar{\xi}_{nb}^{ref}(i,j)}{\partial \bar{T}_p} B_{nb}^{ref}(j) \quad (C2)$$

$$C_{i,j,p}^{ref} = \sum_{nb=1}^{N_b} \frac{\partial \bar{\xi}_{nb}^{ref}(i,j)}{\partial \bar{T}_p} \frac{\partial B_{nb}^{ref}(j)}{\partial \bar{T}_j} \quad (C3)$$

$$D_{i,j,p}^{ref} = \sum_{nb=1}^{N_b} \frac{\partial \bar{\xi}_{nb}^{ref}(i,j)}{\partial \bar{T}_p} B_{nb}^{ref}(i) \quad (C4)$$

$$E_{i,j,p}^{ref} = \sum_{nb=1}^{N_b} \frac{\partial \bar{\xi}_{nb}^{ref}(i,j)}{\partial \bar{T}_p} \frac{\partial B_{nb}^{ref}(i)}{\partial \bar{T}_i} \quad (C5)$$

900 As these last four coefficients do not depend on the narrow-band index, if only the dominant
 901 NERs are considered, then the storage requirement is very small compared to that of $\bar{\xi}_{nb}^{ref}(i,j)$.
 902 Such a parameterization upgrade is therefore easy to implement.

903 However, as soon as the temperature perturbations are of the same order as the difference
 904 $|\bar{T}_j - \bar{T}_i|$ (which can commonly occur for layers close the one to the other), this approximation can
 905 easily lead to a violation of the reciprocity principle. Nothing ensures indeed that the difference
 906 $B_{nb}^{ref}(j) + \frac{\partial B_{nb}^{ref}(j)}{\partial \bar{T}_j}(\bar{T}_j - \bar{T}_j^{ref}) - B_{nb}^{ref}(i) - \frac{\partial B_{nb}^{ref}(i)}{\partial \bar{T}_i}(\bar{T}_i - \bar{T}_i^{ref})$ is positive when \bar{T}_j is greater than \bar{T}_i .
 907 This solution can therefore only be applied to long distance net-exchanges. In practice, we only
 908 used it for net-exchanges with space. It could certainly be used for net-exchanges with the top
 909 of the clouds, for layers far enough from the cloud, but we could not yet think of a systematic
 910 enough procedure.

911 For adjacent layers, a simpler procedure can be implemented. The temperature difference
 912 between adjacent layers can indeed be assumed to be small enough so that the Planck function
 913 can be linearized around the same temperature for the two layers. This leads to

$$\begin{aligned}
\Psi(i, i+1) &= \sum_{nb=1}^{N_b} \Psi_{nb}(i, i+1) \\
&\approx \sum_{nb=1}^{N_b} \bar{\xi}_{nb}^{ref}(i, i+1)(B_{nb}(i+1) - B_{nb}(i)) \\
&\quad + \sum_{p=i}^{i+1} F_{i,i+1,p}^{ref}(\bar{T}_p - \bar{T}_p^{ref})(\bar{T}_{i+1} - \bar{T}_i)
\end{aligned} \tag{C6}$$

914 with

$$F_{i,i+1,p}^{ref} = \sum_{nb=1}^{N_b} \frac{\partial \bar{\xi}_{nb}^{ref}(i, i+1)}{\partial \bar{T}_p} \frac{1}{2} \left(\frac{\partial B_{nb}^{ref}(i)}{\partial \bar{T}_i} + \frac{\partial B_{nb}^{ref}(i+1)}{\partial \bar{T}_{i+1}} \right) \tag{C7}$$

915 The fact that the difference $(\bar{T}_{i+1} - \bar{T}_i)$ appears directly in the expression of the correction terms
916 insures that the reciprocity principle is satisfied whatever the temperature perturbation profile.